DETERMINING THE RELATIONSHIP BETWEEN THE GARLOCK FAULT AND THE EASTERN CALIFORNIA SHEAR ZONE THROUGH DETAILED DIGITAL MAPPING AND AGE CHARACTERIZATION OF FAULTED LANDFORMS, SOUTHEASTERN CALIFORNIA.

A Thesis
Presented to
the Faculty of the Graduate School
at the University of Missouri - Columbia

In Partial Fulfillment
of the Requirements for the Degree
Master of Science

By
Taylor Murphy
Assistant Prof. Tandis Bidgoli, Thesis Supervisor
JULY 2023

The undersigned, appointed by the dean of the Graduate School, have examined the
thesis entitled

DETERMINING THE RELATIONSHIP BETWEEN THE GARLOCK FAULT AND
THE EASTERN CALIFORNIA SHEAR ZONE THROUGH DETAILED DIGITAL
MAPPING AND AGE CHARACTERIZATION OF FAULTED LANDFORMS,
SOUTHEASTERN CALIFORNIA.

presented by Taylor Murphy,

a candidate for the degree of Master of Science,

and hereby certify that, in their opinion, it is worthy of acceptance.

Assistant Professor Tandis Bidgoli

Professor Francisco Gomez

Associate Professor Brent L. Rosenblad

ACKNOWLEDGEMENTS

Primarily, I would like to extend my profound gratitude to my thesis advisors. Tandis Bidgoli, who worked with me from halfway across the country, this project would not have been possible without your guidance, support, and direction; and Francisco Gomez who's guidance, particularly on the remote sensing aspects of this project, allowed me new insight and understanding into a field of science I had not yet explored. I would also like to thank Sean Polun for his contributions to the data analysis in Python, without your code this project would be lacking significantly in data. Finally, I would like to thank my thesis committee, including previously mentioned Tandis Bidgoli and Franciso Gomez, and also including Brent Rosenblad. Thank you all for your patience and feedback on my thesis work.

I am also extremely thankful for funding provided by the National Science Foundation (award 2233310), the Geological Society of America (grant 13586-22), and the University of Missouri Geology Department. I am incredibly thankful for these funds, as they have provided me the opportunity to undergo this research. Additionally I would like to also acknowledge the source of LiDAR data, of which the material is based on services provided to the Plate Boundary Observatory by NCALM (http://www.ncalm.org). PBO is operated by UNAVCO for EarthScope (http://www.earthscope.org) and supported by the National Science Foundation (No. EAR-0350028 and EAR-0732947).

TABLE OF CONTENTS

LIST OF FIGURES

LIST OF TABLES

DETERMINING THE RELATIONSHIP BETWEEN THE GARLOCK FAULT AND THE EASTERN CALIFORNIA SHEAR ZONE THROUGH DETAILED DIGITAL MAPPING AND AGE CHARACTERIZATION OF FAULTED LANDFORMS, SOUTHEASTERN CALIFORNIA.

Taylor Murphy

Dr. Francisco Gomez Thesis Supervisor

ABSTRACT

Southeastern California is known for complex fault networks that accommodate strain from Pacific-North American plate convergence. The 250-km-long, left-lateral Garlock fault is integral to this system, yet its overall kinematic role within the plate boundary and relationship with faults of the Eastern California shear zone/Walker Lane belt remain poorly understood. A key area that has not been adequately studied is a 15-km stretch of the eastern Garlock fault, at its intersections with the right-lateral Brown Mountain fault and left-lateral Owl Lake fault. This segment of the fault lies within the China Lake Naval Air Weapons Station and U.S. Fort Irwin boundaries, which have restrictions on civilian access and portions of which contain unexploded ordnance, making them unsuitable and unsafe for field investigations. The purpose of this project is to use a combination of high-resolution LiDAR topographic data, remotely sensed imagery, and published geochronology data to map and establish the ages of faulted landforms along this portion of the eastern Garlock fault. The inaccessibility of this area makes it ideal for the application of remote-sensing techniques.

A range of surface analysis techniques were used to differentiate and map Quaternary units in the study area. Geomorphic surface properties were determined from physiographic

roughness and surface reflectance data, established from analysis of LiDAR, radar backscatter, and visual-near and short-wave infrared multispectral and hyperspectral reflectance datasets. The ages of faulted landforms were established using two approaches: (1) fault scarp and terrace riser degradation analysis and (2) a surface property-age model that links remotely sensed surface properties to new and published ages of alluvial surfaces in the region. A final goal of the study was to determine the slip rate along this segment of the Garlock fault and other faults in the map area. To accomplish this, offset landforms, such as terrace risers and channels, were analyzed in the context of the new age determinations. The results will be compared to published slip rate estimates for the region in order to better understand the Garlock fault's role within the plate boundary and how plate boundary strain is being accommodated in such an intraplate setting.

1. INTRODUCTION

An infamous interaction between tectonic plates is the collision of the eastern oceanic Pacific plate with the western continental North American plate in current-day California. It is a long standing question in the geosciences about how regional strain is accommodated from the collision of these plates. It is thought that strain along this boundary is accommodated by a large array of different fault networks with a range of kinematic relationships. The relationships between intersecting faults, and their specific motions, can illuminate how regional strain is accommodated. The Garlock fault is a left-lateral fault directly adjacent to the notable and notorious San Andreas fault system. The Garlock system in addition to other adjacent faults, such as the right-lateral Brown Mountain fault, play integral roles in accommodating regional deformation. Figure 1-1 shows the regional geography of the fault systems and their locations relative to one another. The western segments of the Garlock fault have been well-studied (e.g. Carter, 1994; Burbank and Whistler, 1987; Monastero et al., 1997; Keenan, 2000; Rittasse et al., 2014; Dolan et al., 2016) due to the accessibility of field sites, however, the eastern segments are located within restricted and topographically inaccessible regions. Previous studies of the accessible, western segments of the Garlock fault yielded slip rates of 5-7 mm/yr (McGill et al., 2009; Ganev et al., 2012). The slip rate of the western portions, especially in relation to the larger Garlock fault as a whole, has not been studied extensively and is largely debated. To understand the full role of the Garlock fault within the collisional boundary strain system, the strain rate along all segments is necessary.

Currently there are four general models which aim to constrain the relationship of the Garlock fault with the surrounding fault networks (Figure 1-2). The first, the “conjugate fault hypothesis”, asserts that the Garlock fault is conjugate with regional right-lateral faults directly adjacent to the longer Garlock fault. For this hypothesis to be valid, the slip amounts on regional right-lateral fault systems such as the Panamint Valley fault, the southern Death Valley fault zone, and the eastern California Shear zone, should correspond to the left-lateral slip along the Garlock fault (e.g. Hill and Dibblee Jr, 1953). The second model, the "transform fault hypothesis", suggests the larger Garlock fault is acting as an east-west transform fault which accommodates extension from adjacent Basin and Range associated faulting. In this hypothesis, the horizontal extension on faults like the Panamint Valley fault and southern Death Valley fault zone will balance with decreasing slip rate on the eastern segments of the Garlock fault (e.g. Davis and Burchfiel, 1973). A third hypothesis is the "clockwise rotation" model, which proposes that the Garlock fault accommodates the rotation of the Mojave block and conjugate Eastern California Shear zone faults in southern California. The clockwise rotation of the Mojave block would cause left-lateral motion, which we see in the Garlock fault; however, for this hypothesis to hold, the slip rate along the Garlock fault should be consistent across the entire east-west extent (Weldon and Humphreys, 1986). Finally, the "missing fault hypothesis" suggests missing information within the previously mentioned models. This theory indicates that the previous three hypotheses cannot explain the observed motion along the length of the Garlock fault, and that there are structures (i.e. additional faults) that are playing a role in the overall kinematics. These models are not all-encompassing, however they offer interpretations of the motion along the Garlock fault to overall regional kinematics in southern California.

It is the intent of this study to categorize and determine the relative ages of alluvial fan surfaces along the intersection of the southern Brown Mountain fault and eastern segments of the Garlock fault. In order to accomplish this, a detailed digital map of the intersection of the Garlock fault and the Brown Mountain fault will be created using LiDAR and NAIP remotely-sensed data sets. The geographic extent of the map area is approximately 52-km^2, and is shown in Figure 1-1. Using the determined age relationships and measured lateral offsets, the slip rate along this portion of the Garlock fault will be determined.

An additional long-standing problem in geoscience research is the need to accurately date different rock formations. Acquiring an absolute age requires both field and laboratory efforts; from collecting valid test samples to crushing, milling and experimentally testing such samples. These efforts are incredibly time-consuming and require a significant amount of budget resources. Recent studies have shown that remotely-sensed properties of rock formations (i.e. surface roughness) in arid climates can be correlated to absolute age values (Frankel et al., 2007; Regmi et al., 2014). This study will also be used as a tool to calibrate and assess the accuracy of remotely collected data, specifically surface roughness, to determine the absolute ages of alluvial fan surfaces in arid environments.

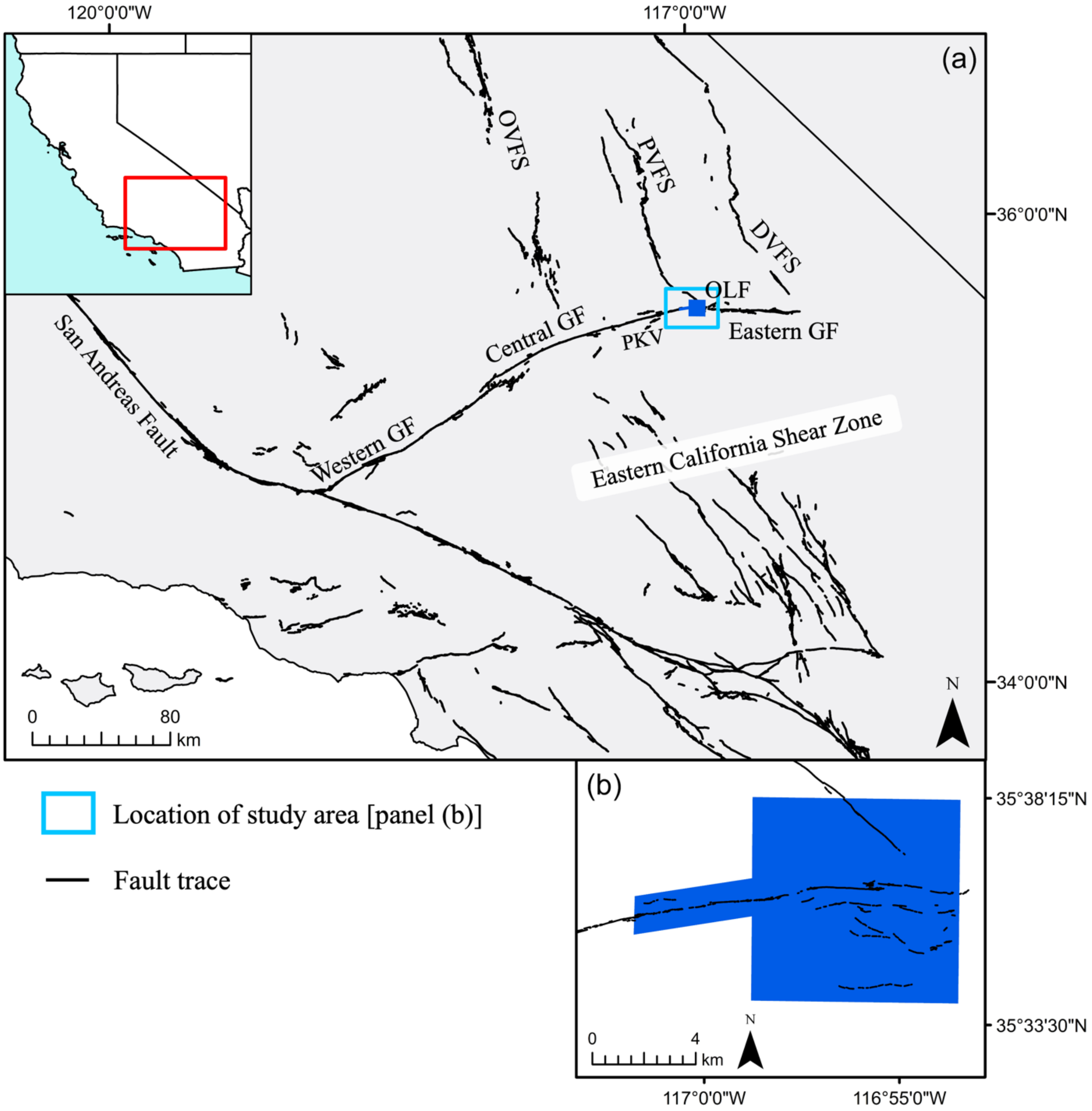

Figure 1-1. (a) Map of southern California regional fault networks; GF: Garlock Fault; OVFS: Owens Valley Fault System; PVFS: Panamint Valley Fault System; DVFS: Death Valley Fault System; OLF: Owl Lake Fault; PKV: Pilot Knob Valley. (b) Map of the study location, the blue highlighted area is the region that is digitally mapped in this study.

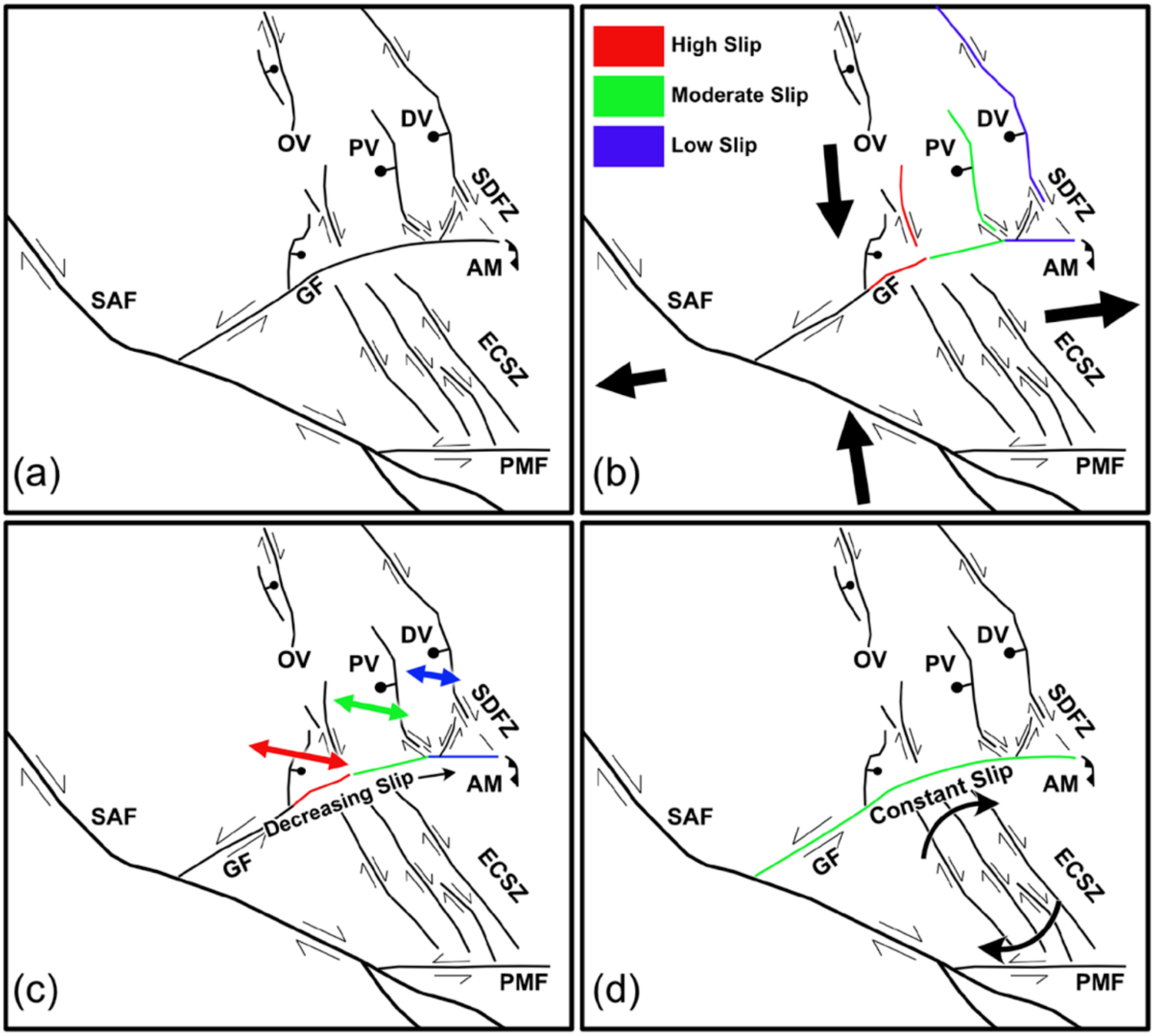

Figure 1-2. (a) Map of larger fault systems in southern California: SAF, San Andreas fault; GF, Garlock fault; PV, Panamint Valley fault; DV, Death Valley fault; SDFZ, Southern Death Valley fault zone; ECSZ, Eastern California Shear zone; OV, Owens Valley fault zone; PMF, Pinto Mountain Fault; Avawatz Mountain fault; (b) 'Conjugate fault' model: adjacent right-lateral faults have similar slip rates to the Garlock fault; (c) 'Transform fault' model: slip rate of the eastern Garlock fault corresponds to adjacent extension from the Basin and Range province; (d) 'Clockwise rotation' model: the rotation of the Mojave block induces constant slip on entire length of the Garlock fault. *From Sean Polun*

2. GEOLOGIC BACKGROUND

The geology of eastern California is complex, with a number of orogenic events overprinting the region and creating distinct provinces of deformation. Deformation in eastern California is still on-going along the western margin of the North American plate and in regions inboard of the San Andreas fault, adding another layer of deformation to scrutinize when attempting to understand the history and current configuration of each tectonic element.

2.1. Garlock Fault

The approximately 250-km, left-lateral Garlock fault is understood to be a major tectonic element in southern California in accommodating the plate boundary strain. Initial movement along the fault in the middle to late Miocene time, however the slip rate along the entirety of the fault length is still the subject of many research studies (e.g. McGill et al., 2009; Ganev et al., 2012; Andrew et al., 2014a, 2014b; Barnhart et al., 2019). Additionally, the fault itself is unique in that along its scarp, it does not appear to be offset or be offset by the surrounding north-northwest trending Eastern California shear zone fault system (Frankel et al., 2008). Behaviorally, the fault is commonly divided into two major segments, the 150 km western segment and 100 km eastern segment. The western segment of the Garlock fault has been extensively studied (Carter, 1994; Burbank and Whistler, 1987; Loomis and Burbank, 1988; Monastero et al., 1997; Meade and Hager, 2005; Rittasse et al., 2014), and describes the relatively northeast-southwest trending section adjacent to the San Andreas fault. Radiocarbon dating in the central region of the Garlock fault, within Searles Valley, offers a range of 4-9 mm/yr as the slip rate (McGill and Sieh, 1993).

The eastern segment begins as the fault bends southward and becomes east-west trending. This section of the Garlock fault is much less accessible, and has therefore been neglected in many research studies. Analysis of exposed rock, aged 12-11 Ma, along the Garlock fault yielded an offset of ~30 km; implying the initial motion along the Garlock fault was as high as 10 mm/yr from 15-12 Ma (Frankel et al., 2008). Present spatial relationships between measured offset exposed geologic units in the Red Rock Canyon and the Summit Range of eastern California found approximately 35 km of offset since the initial incipient movement. This offset suggests a slip rate of only 2.75-3.0 mm/yr averaged over the past 11 million years (Frankel et al., 2008). There is much variability found in different studies along the length of the Garlock fault. More recent studies have dated lateral offsets using infrared-stimulated luminescence and found the Holocene slip rate of the Garlock fault was larger than 14 mm/yr (Dolan et al., 2016). Understanding the variability of slip along the Garlock fault may illuminate the relationships between the surrounding structures and strain accommodation within the region.

Seismically, the Garlock fault has not produced any large-scale earthquakes within the timeframe of recorded human history. However, there is geologic evidence that suggests it has ruptured in large events in the past. Studies document the most recent ruptures along the western segment at 890 ± 195 ^{14}C yr B.P., and in the central segment in Searles Valley in 1490 A.D. (LaViolette et al., 1980; McGill, 1993). From the observed offsets along the fault it is estimated these large earthquakes produced moment magnitudes of between 6.6 to 7.8 (McGill and Sieh, 1993). Paleoseismic studies have estimated recurrence intervals for surface-rupturing events along the entirety of the Garlock fault between 200 and 1700 years (e.g. LaViolette et al., 1980; Smith, 1979).

While not unique to the Garlock fault, the large and complex arrays of fault networks in southern California produce discrepancies between observed geologic slip rates and estimated geodetic slip rates (Guns et al., 2020). Along the Garlock fault, GPS slip rate estimates are up to

1.5-2 times slower than calculated geologic rates (Chuang and Johnson, 2011). It is imperative to investigate the Garlock fault system in detail in order to reconcile the observed differences in slip rate, and to resolve the overall kinematics of the southern Californian region.

2.2. The Eastern California Shear Zone

Located east of the North American-Pacific plate boundary, a region of primarily right lateral, north-norwest trending strike-slip faulting occurs across eastern California and into southwestern Nevada. This region has been named the Eastern California shear zone (ECSZ). The region of active faulting and deformation spans from the large southeastern bend of the San Andreas fault, south of the Garlock fault, and through the Mojave Desert to the western margin of the Basin and Range province (Frankel et al., 2008). The ECSZ plays an integral role in the accommodation of strain from the North American-Pacific plate collision, it is thought that the ECSZ accommodates ~20-25%, or 9.3 ± 0.2 mm/yr, of the total relative motion between the two tectonic plates (Bennett et al., 2003; Frankel et al., 2008).

Geologic offsets along the right-lateral faults and geodesy estimates suggest a minimum age of two to four million years, with an overall age estimate of at least 10 million years (Miller et al., 2001). Regional studies have correlated Jurassic and Cretaceous dikes, Cretaceous leucogranites, and a Devonian marine channel, suggesting a much older age of inception of at most 83 Ma (Bartley et al., 2007; Glazner et al., 2005; Kylander-Clark, 2003).

Seismicity in the region is relatively limited (Figure 2-2). Within the ECSZ there have been six large earthquakes, exceeding magnitude (M_w) 6.8 since 1872: (1) Owens Valley, 1872; (2) Pleasant Valley, 1915; (3) Cedar Mountain, 1932; (4) Dixie Valley-Fairview Peak, 1954; (5) Landers, 1992; and (6) Hector Mine, 1999 (Miller et al., 2001). In the northern region of the ECSZ displacement occurs along four larger fault systems: the Death Valley-Fish Lake Valley, Panamint Valley-Hunter Mountain-Saline Valley, Owens Valley, and Stateline fault systems (Frankel et al., 2008). Most of the faults in the region show little to no evidence of recent activity, and the estimated recurrence interval for magnitude 6.8 or above along the aforementioned individual faults in the region is over one thousand years (Miller et al., 2001). There is evidence that the major fault systems in the region (e.g. Figure 1-1; Death Valley fault zone, Panamint Valley fault zone, Owens Valley fault zone) may rupture together as “clusters” in the northern ECSZ (McAuliffe et al., 2013).

From the Pleistocene to recent time, the regional rate of right-lateral shear along the four main fault systems has remained relatively constant at 9-10 mm/yr; however there is still uncertainty in the slip rates of the Owens Valley and Panamint Valley–Hunter Mountain–Saline Valley faults (Bennett et al., 2003; Bacon and Pezzopane, 2007; Frankel et al., 2008). Across the left-lateral Garlock fault, slip near the U.S. Army Base Fort Irwin is estimated to be 6-7 mm/yr northward into the Death Valley region (Miller et al., 2001). Partitioning of this slip onto the northwest striking right-lateral faults in combination with the east-west striking left-lateral faults is still the subject of current research.

2.2.1. The Death Valley-Furnace Creek Fault Zone

The dextral Death Valley-Furnace Creek fault zone (DVF) to the north of the eastern Garlock fault is a major segment of the Eastern California shear zone, and is thought to accommodate significant strain from the Pacific-North American plate boundary collision (Figure 1-1; Frankel et al., 2007). This fault system is typically separated into a north-south striking northern section and a northwest-southeast striking southern segment spanning for more than 115 km along the western edges of the Grapevine Mountain and Black Mountain ranges through Death Valley National Park (Butler et al., 1988). The 170 km northwest-southeast striking Furnace Creek fault is believed to be an extension of the northern Death Valley fault system along the western margin of the Funeral Mountain range (Snow and Wernicke, 1989). It is thought that all three segments- the northernmost Furnace Creek fault, the northern Death Valley fault zone, and the southern death valley fault- are related to extension attributed to the Basin and Range province kinematics; and it is thought the movement along the structures created the pull-apart basin that is Death Valley (Butler et al., 1988). This ~250 km long extensive regional structure is believed to terminate in the south as it intersects with the east-west striking Garlock fault (Butler et al., 1988).

The regional slip rate along the entirety of the Death Valley-Furnace creek system has been shown to be geographically variable. Additionally, there is debate over the magnitude of slip along the structure. Studies have documented a minimum offset of 30 km to a maximum of 63 km along the Death Valley fault system due to discrepancies on correlation of offset features (Butler et al., 1988; Miller et al., 2001; Renik and Christie-Blick, 2013). The large difference between the minimum and maximum determined magnitudes of offset have made it difficult to determine the slip rate along these fault systems. Butler et al. (1998) determined a slip rate on the northern section of the Death Valley fault over the last 3-5 million years to be 5 mm/yr; whereas Frankel et al. (2007) dated offset alluvial fan surfaces from northern Death Valley have been dated using Be^{10} analysis and determined a slip rate of 2.5-3 mm/yr. GPS data modeling of the northern Death Valley fault zone suggests a storage of strain at a rate of 4-10 mm/yr; the geologic slip rate from the same region, calculated from offset alluvial fan units and Be^{10} and Cl^{36} ages, is 4.85 ± 1.06 mm/yr (Frankel et al., 2007). The variability in the slip lies in the northern and southern terminus of the fault system. It is agreed upon that toward the ends of the fault system the slip rate decreases; north in Fish Lake Valley, the geologic slip rate has been documented to slow to 2.5-3 mm/yr (Frankel et al., 2007; Renik and Christie-Blick, 2013).

2.2.2. The Owl Lake Fault

Intersecting the central Garlock fault in the north is the northeast-southwest striking, left-lateral oblique-slip Owl Lake fault. The 19-25 km-long Owl Lake fault branches out from the Garlock fault into the southern Panamint Mountain range and Death Valley region. McGill (1993) observed offset observed fanglomerate units and dated organic matter from alluvial units found along the Owl Lake fault to estimate a sinistral slip rate of 1-3 mm/yr.

This structure is not well studied, and unique to the region in its strike and sense of motion. The Owl Lake fault does not follow the dominant strike nor right-lateral motion of the surrounding Eastern California shear zone. This orientation and dynamics of the Owl Lake fault structure suggests it may play a key role in the accommodation of strain either directly or indirectly from the larger Garlock fault.

2.2.3. The Panamint Valley Fault Zone

The second major fault system within the northern Eastern California Shear Zone is the Panamint Valley fault zone (Figure 1-1). Similarly to the Death Valley-Furnace Creek fault zone, the Panamint Valley fault zone is understood to have originated as an extensional, detachment structure approximately 15 million years ago (McAuliffe et al., 2013). Both structures were active parts of the Basin and Range Province, specifically named the Death Valley Extensional Region, during the Neogene and Quaternary periods (Zhang et al., 1990). Due to a shift in the kinematics of the region, the Panamint Valley fault zone transitioned from low angle normal faulting to dextral strike-slip faulting four million years ago, aligning itself with the regional motion of the surrounding Eastern California shear zone (McAuliffe et al., 2013).

Geographically, the Panamint Valley fault zone strikes north-northwest for 95 km along the western edge of the Panamint Mountain range, west of Death Valley. The fault system includes the Hunter Mountain fault, a 40 km dextral fault, to the north; and the Brown Mountain fault, a 13 km dextral fault, in the south. The Brown Mountain fault intersects with the Garlock fault at its southern terminus, and is one of the main structures featured in the mapping of this project.

Presently, the seismicity in the region is relatively low. Earthquake epicenter maps from 1900-1970 show sporadic, small events with no evidence of any large earthquake events (Hileman et al., 1973). The slip rates within the Panamint Valley fault zone, like the Death Valley fault zone, are variable depending on the geographic location. The northern region of the fault zone, along the Hunter Mountain fault, has a documented slip rate of 2-3 mm/yr averaged over the past 3 million years (SCEDC, 2023). Studies of the Panamint Valley fault document displaced alluvial units dated to the Pleistocene with 9 ± 1 km of offset, yielding a minimum slip rate of 1.74 ± 0.65 mm/yr (Zhang et al., 1990; Andrew and Walker, 2009). However, as you go south along the Panamint Valley fault, into the Brown Mountain fault zone, this slip rate increases slightly to 1.75–2 mm/yr (Hoffman et al., 2009).

2.2.4. Owens Valley Fault Zone

Located directly north of the Garlock fault, near the city of Lone Pine, California, is the Owens Valley fault zone (OVF). It is argued that the OVF is one of the primary dextral shear structures accommodating a large portion of strain in the Eastern California shear zone (Figure 1-1; Kirby et al., 2008). This region of fault structures is characterized by 100 km of linear scarp arrays in the central Owens Valley with 6 ± 2 m of right-lateral slip from the most recent rupture event (Beanland and Clark, 1982). This most recent event is the largest historic earthquake on record in the Basin and Range Province and the third largest magnitude earthquake in the contiguous United States, with a magnitude of 7.5-7.75 (Bacon and Pezzopane, 2007). Paleoseismic studies of the history of the Owens Valley fault zone (e.g. Lubetkin and Clark, 1988; Beanland and Clark, 1982; Lee et al., 2001; Bacon and Pezzopane, 2007) have estimated a recurrence interval between 3–5 kyr.

Regional GPS velocities are variable within the region (Figure 2-1). Geodetic data suggest slip rate across Owens Valley should be 5–7 mm/yr; however, recent studies in the area (e.g. Bacon and Pezzopane, 2007; Kirby et al., 2008) yield a relatively low slip rate through the central section of the Owens Valley fault zone. These studies found slip in the region to be as low as 1.0 ± 0.5 mm/yr, and between 2.8 – 4.5 mm/yr over the past 55 – 80 kyr, respectively.

2.2.5. Mojave Desert Block

The southern portion of the Eastern California shear zone, understood to be south of the east-west striking Garlock fault, is the region known as the Mojave Desert block. This region is a wedge-shaped block bounded in the west by the San Andreas fault, in the north by the Garlock fault, to the west by the Avawatz Mountain range, and in the south by the Pinto Mountain fault (Dokka, 1986). The Mojave block also lies directly adjacent to the Basin and Range province to the east.

The fault history of the Mojave block is complex; it consists of northwest striking right-lateral ECSZ faults, combined with westernly striking left-lateral faults, and apparent clockwise rotation of the entire block (Glazner et al., 2002). The kinematics of the Mojave Block are complex and largely debated. There is controversy surrounding the magnitude, distribution, and relative timing of the strain partitioning along the faults in the region (Shermer et al., 1996). The north-northwest striking faults are thought to accommodate, most recently, late Tertiary slip and heterogeneous clockwise rotation associated with the plate boundary interaction; it is thought the Mojave block has been accommodating strain from the plate boundary for the past ten million years (Shermer et al., 1996; Miller et al., 2001). Just south of the Garlock fault, geodetic studies have estimated the summed slip rate of these faults to be 7.0 +/- 0.6 mm/yr (McGill, 2015).

Seismically, the region has been shown to be active in clusters of earthquakes. The last 12,000 years the seismic strain release has been documented to occur in clusters of large earthquake events (Rockwell et al., 2015; Ganev et al., 2010). Paleoseismic data reveal historical clusters of earthquakes at ~8–9.5 ka and 5–6 ka, as well as a current cycle for the past 1.0–1.5ka (McAuliffe et al., 2013). The current cycle includes famous historical earthquakes, such as the Landers earthquake in 1992, M_w 7.3, and the Hector Mine earthquake in 1999, M_w 7.1 (Rockwell et al., 2015). There is also evidence that the faults within the northern Eastern California shear zone, the Garlock fault, and the faults within the Mojave block may rupture as a system in “megaclusters” associated with strain from the Pacific-North American plate collision (McAuliffe et al., 2013).

Figure 2-1. Global Positioning System (GPS) crustal velocity map of southeastern California around the regional tectonic regions. Data source is Global Navigation Satellite System (GNSS) N. America, NAM14, UNAVCO. Map created from EarthScope Consortium's Geodetic Facility for the Advancement of Geoscience (GAGE). https://www.unavco.org/software/visualization/GPS-Velocity-Viewer/GPS-Velocity-Viewer.html.

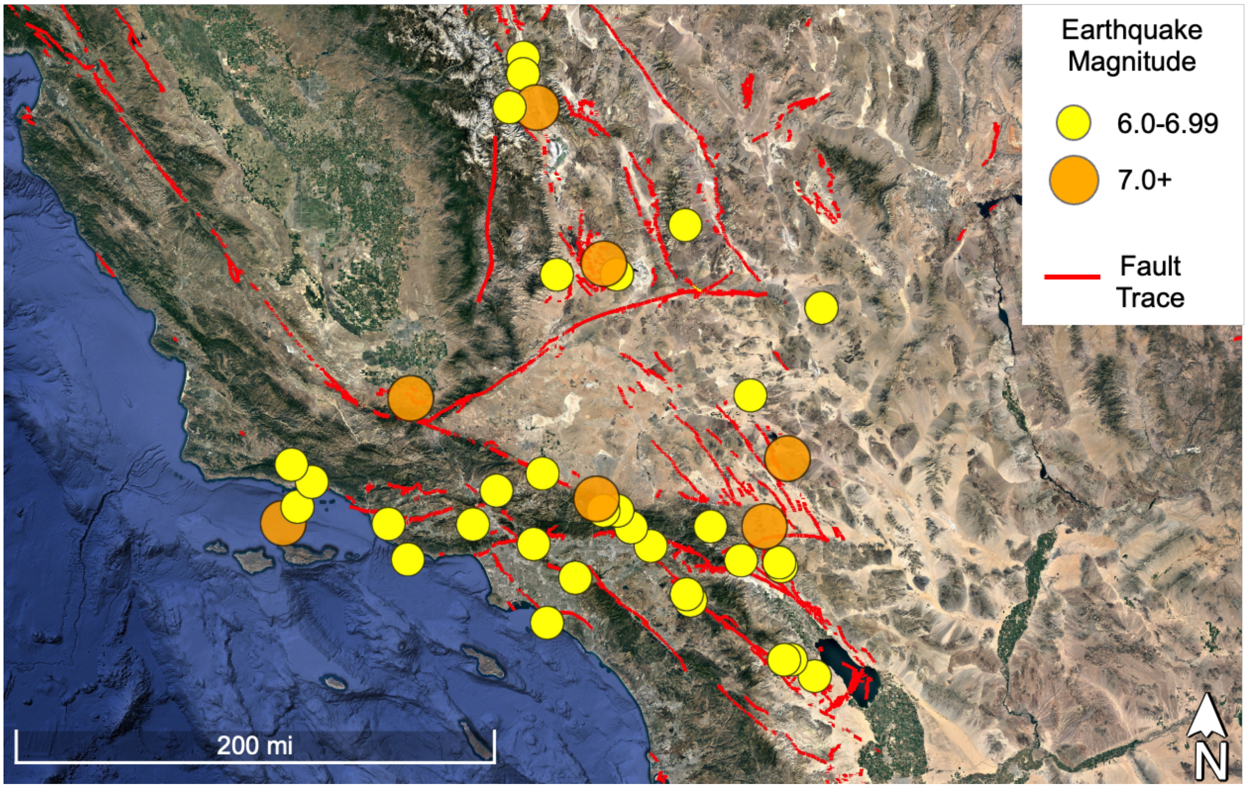

Figure 2-2. Historical earthquake map of southern California. Earthquakes filtered to show events at a magnitude of 6.0 or higher from the years 1700-2020. Yellow circles show earthquake events of magnitude 6.0-6.99, orange circles are magnitude 7.0 or higher. Data compiled from the USGS Earthquake Catalog. https://earthquake.usgs.gov.

3. METHODS

3.1. Digital Mapping

The region of intersection between the Brown Mountain fault and the Garlock fault is inaccessible to field work due to treacherous terrain and United States military ordinances. In order to remove the obstacle of in-person field work, a 52 square kilometer area of the intersection between the Garlock and Brown Mountain faults was digitally mapped using remotely-sensed data sets and the ESRI ArcGIS geospatial processing software (ArcMap v. 10.1.7). LiDAR (Light Detection and Ranging) and NAIP (National Agriculture Imagery Program) data sets were used to differentiate structures and geologic units in the map region. From the finished mapping product, offset alluvial fan surfaces were analyzed to determine offset distances and relative timing between alluvial units.

3.1.1. NAIP Analysis

The national NAIP imagery database is collected by the U.S. Department of Agriculture's (USDA) Farm Service Agency, originally with the intention to capture aerial imagery for agricultural purposes. NAIP is a passive remote sensing method, meaning the sensors used to capture the data utilize the natural sunlight to capture radiation off the earth's surface. This data set is open-source and readily available to the public, and can be utilized in many different areas of study. The NAIP images used for this study are 3.75-minute longitude x 3.75-minute latitude quarter quadrangle. The aerial imagery is captured at a resolution of 1-meter ground sample distance (GSD) in natural color; natural color refers to a four-band window of captured wavelengths red (600–700), green (500–600 nm), blue (400–500 nm), and near infrared (800–900 nm).

NAIP quadranges captured in between May 15, 2020 to May 23, 2020 were used to delineate structures and alluvial units within the map area. The true-color nature of the aerial imagery allows for units to be differentiated based on the observable color of alluvium. Additionally, the passive acquisition nature of the imagery allows for natural shadows and relief between structures to stand out. These indicators were used to delineate the alluvial units in the mapping region (Figure 3-1).

3.1.2. LiDAR Analysis

An additional data set that was used to complete the digital mapping product is a LiDAR digital elevation model (DEM). Unlike NAIP imagery, LiDAR is an active remote sensor– the equipment uses its own source of light to reflect off the ground surface. Typically, LiDAR sensors use near infrared wavelengths (750 nm to 1.5µm) to collect data. The LiDAR survey used to create the digital mapping product was collected in April, 2007 and the produced raster DEM has a point density of 4.61 pts/m^2, and a raster resolution of 0.5 meters (SECLP, 2007). While open and accessible to the public, LiDAR data sets are not comprehensive over the entire earth's surface. Of this project's map area, the accessed LiDAR data set covers approximately 52 km^2. The LiDAR digital elevation model was used to create a shaded relief model, or "hillshade", in which lighting effects are applied to the topography. "Hillshade" maps add illumination, shading, and shadows, giving a three-dimensional view of the topographic features. Using the ArcToolbox "Spatial Analyst" tool a hillshade was created with a sunlight azimuth of 315° from north and altitude of 25° from the horizon (Figure 3-2).

Models which include lighting effects are essential to the digital mapping production, the extracted data is projected in black and white, which allows the bias of color to be eliminated and for the topographic and morphological features of the region to stand out. Identified structures that are highlighted from the LiDAR hillshade include, but are not limited to, fault traces, incised alluvial channels, laterally offset landforms, and vertical relief.

3.1.3. Surface Roughness Analysis

In arid regions, where the land surface cover consists of alluvial fans, a distinguishing characteristic of the age of an alluvial fan is the roughness of its surface. In these dry climates with intense sun exposure (i.e. deserts), the exposed rock on alluvial fan surfaces develop a “desert varnish” layer of magnesium oxide. An additional characteristic of alluvial fans is their topological progression over time. It has been shown that as alluvial fans age, their topography progressively smooths (Frankel et al., 2007). The magnitude of the topological smoothing can be captured by remote sensing techniques, making it possible to identify relative ages of alluvial fans through aerial imagery. The use of surface roughness analysis to determine the differences in alluvial fan surfaces is widely used and applied to research studies (e.g. Frankel et al., 2007; Su et. al, 2022). The availability of LiDAR data makes calculating the surface roughness of alluvial fans a relatively easy and practical method of delineating different age relationships. By definition, surface roughness is the standard deviation of the topography, or slope, in a given neighborhood (Figure 3-4). The surface roughness map (Figure 3-5) was calculated using the 0.5-m-resolution LiDAR digital elevation model, first by using ArcToolbox software Raster Surface tool to create a slope map of the region (Figure 3-3). The slope, m,was calculated in a 3 by 3 meter moving window, defined by

$$m = tan^{-1}\sqrt{(\frac{\delta z}{\delta x})^2 + (\frac{\delta z}{\delta y})^2} \qquad (1)$$

where $\frac{\delta z}{\delta x}$ is the maximum slope in the north-south direction; $\frac{\delta z}{\delta y}$ is the maximum slope in the east-west direction; and z is the elevation of the ground surface (Frankel et al., 2007).

The output is a raster data set where the slope of the neighborhood's topography is reported in degrees. Then, from the slope map, the standard deviation of the vectors were calculated in a 3 x 3 pixel neighborhood using the ArcToolbox Spatial Analyst "Focal Statistics" tool, calculated using equation

$$\sigma_m = \sqrt{\frac{\sum_{i=1}^{n} (m_i - \underline{m})^2}{n}} \tag{2}$$

where σ_m is the standard deviation of the slope, or surface roughness; n is the number of samples in the population, which is nine for the 3x3 calculation; $m_i$is a slope value calculated in equation (1) within the sampling area; and $\underline{m}$ is the mean slope value (Frankel et al., 2007).

3.2. Lateral Offset Analysis

An integral part of calculating fault slip rate is identifying the magnitude of offset the fault has experienced. In order to measure the amount of offset along identified fault segments, offset landforms were first identified from the mapping product. To verify the identified landforms are the same across the fault, the offsets were restored to pre-faulted configurations. Anchoring points within each landform were then identified on each side of the fault. To quantify the lateral distance, the "Measure" tool in ArcGIS was utilized. In this measurement, the reported value is the distance between established anchoring points. Errors in this measurement come from multiple sources. Error inherently exists in the creation of the map and the data sets used, as well as the tool used in the ArcGIS software to measure the offset. Morphology of the measured landform also plays a role in the errors of measured offset. One major source of error is erosion of the landforms. Measuring landforms exposed to significant erosion would cause the landform to be reported as having a larger offset than the lateral movement of the fault itself. To account for these errors in the map, morphology, and ArcGIS tool, values are reported as the minimum and maximum, and the average.

3.3. Scarp Degradation Analysis

The second value needed to calculate an accurate slip rate is the time elapsed between the rupture events on the fault. For this project, the time between rupture events was determined using scarp degradation analysis. Landform evolution describes the changes in topology of features in both space and time; which is a function of tectonic processes, weather events, regional climate, erosion, and depositional events. A fault scarp is a steep, linear slope caused by the tectonic movement of fault surfaces. While named "scarp" analysis, in addition to fault scarps, landforms with similar scarp morphologies can also be modeled using this technique. In this study, both fault scarps and terrace risers are analyzed. Using the LiDAR digital elevation model, scarp profiles that are perpendicular to the fault trace and that avoid local channels and gullies can be extracted from the map area and reliably analyzed (Hanks et al., 1984). The degradation of these landforms over time can be mathematically modeled using the homogeneous equation

$$\frac{\delta u}{\delta t} - \kappa \frac{\delta^2 u}{\delta x^2} = 0 \qquad (3)$$

where u is the elevation of the scarp; $\delta u/\delta t$ is the rate of change of the elevation; $\delta^2 u/\delta x^2$ is the curvature of the fault scarp; and κ is the mass diffusivity constant of the region, typically reported in square meters per kiloannum (m^2/ka) (Hanks, 2000). The mass diffusivity constant is dependent on the climate, and must be calibrated to reflect the consolidation of mass in individual region (Hanks et al., 1984). The relationship in equation (3) states that when topography is concave up ($\delta^2 u/\delta x^2 > 1$) elevation will increase with time, contrasting when topography is concave down ($\delta^2 u/\delta x^2 < 1$) elevation will decrease with time; and that topography with sharper angles will degrade faster than smoother topography with the same mass diffusivity constant (Hanks, 2000).

The solution to this differential equation varies depending on the nature of a particular fault's kinematics. For a single event of vertical, dip-slip fault rupture, the solution becomes

$$u(x,t) = a\ erf(\frac{x}{2\sqrt{\kappa t}}) + bx \tag{4}$$

where u is the elevation; a is half of the surface offset, $2a$; $erf(v)$ is the error function of the argument v; b is the slope of the scarp; and x is the cross-strike distance (Hanks, 2000). For a scarp that has undergone multiple faulting events becomes

$$u(x,t) = (\alpha + At)\ erf(\frac{x}{2\sqrt{\kappa t}}) + \frac{Ax^2}{2\kappa}\{\ erf(\frac{x}{2\sqrt{\kappa t}}) - sgn(x)\} + \frac{Ax}{\kappa}\sqrt{\frac{\kappa t}{\pi}}\, e^{\frac{-x^2}{4\kappa t}} + bx \tag{5}$$

where α is the tangent of the angle of repose for the sediment; A is the velocity of the uplift or downdrop; and the $sgn(x)$ argument is dependent on whether the scarp is undergoing uplift or downdrop, such that

uplift $\quad x > 1 \quad sgn(x) = 1$ (6)

downdrop $\quad x < 1 \quad sgn(x) = -1$ (7)

and for all values of x, both α and A are positive (Hanks et al., 1984). Both models (single event versus multiple event) should be considered end-members of a fault's behavior unless there is unambiguous geologic evidence for a single event (Hanks et al., 1984). For the analyzed scarp profiles, both single and multiple event rupture models were used to analyze the extracted data. It was individually determined for each profile which uplift analysis better fit the geologic constraints.

The application of these models was done using a Python code, "PyScarpFit" (https://github.com/seanpolun/pyScarpFit). This code located the midpoint of the identified scarp, where $x = 0$, and uses the solution equation to identify the magnitude of throw on the fault scarp, $2H$, and the value of α (Figure 3-5). Using the known value of κ for the region, the time it has taken for a scarp to arrive at its current shape can be calculated (Hanks et al., 1984).

For this study, κ was not measured or tested for, instead, the κ used for fault scarp age calculations was calibrated using studies that were undergone in areas with similar climates to the mapping region. κ is dependent on the annual magnitude of rainfall, thus a study focused on a field site with similar amounts of annual precipitation will yield the most accurate κ value. The town closest to the mapping location, Ridgecrest, California, reports a precipitation rate of 0.17 mm/day, which corresponds to an annual precipitation rate of 62.05 mm/yr, Frankel et al. (2015) completed a study in Badwater Basin within Death Valley National Park; this region has an average annual rainfall of 50 mm/yr (NPS, 2023). Both in proximity to the mapping region, and in rainfall magnitude, the Frankel et al. (2015) study is a good approximation for the κ value of the mapping area. The κ value was calculated by dating alluvial fan surfaces using Optically Stimulated Luminescence (OSL) and scarp profile modeling, yielding a value of $\kappa = 0.3 \pm 0.1$ m^2/kyr (Frankel et al., 2016). This value is used from this point in all fault scarp degradation calculations.

3.4. Uncertainty and Error Reporting

The described measurements and models innately contain uncertainties and errors in the reported values. In order to account for these uncertainties in subsequent calculations, a Gaussian probability distribution is used

$$\sigma = \left(\frac{1}{(\sigma_1)^2} + \frac{1}{(\sigma_2)^2} + \ldots + \frac{1}{(\sigma_n)^2}\right)^{-1/2} \tag{8}$$

$$\mu = (\sigma^2 ((\frac{\mu_1}{\sigma_1})^2 + (\frac{\mu_2}{\sigma_2})^2 + \ldots + (\frac{\mu_n}{\sigma_n})^2))^{1/2} \qquad (9)$$

where σ represents the standard deviation of measurements; μ represents the mean value of the data set or measurement; and the subscripts 1-n denote the individual measurement (Geyh & Schleicher, 1990).

Given these variables, the expression for the arithmetic rule for the division of normal probability is

$$\frac{\mu_1 \pm \sigma_1}{\mu_2 \pm \sigma_2} = \frac{\mu_1}{\mu_2} \pm \frac{\mu_1}{\mu_2} ((\frac{\sigma_1}{\mu_1})^2 + (\frac{\sigma_2}{\mu_2})^2)^{1/2} \qquad (10)$$

The subsequent values, calculations, and measurements within this project are all treated as data sets with normal probability distributions.

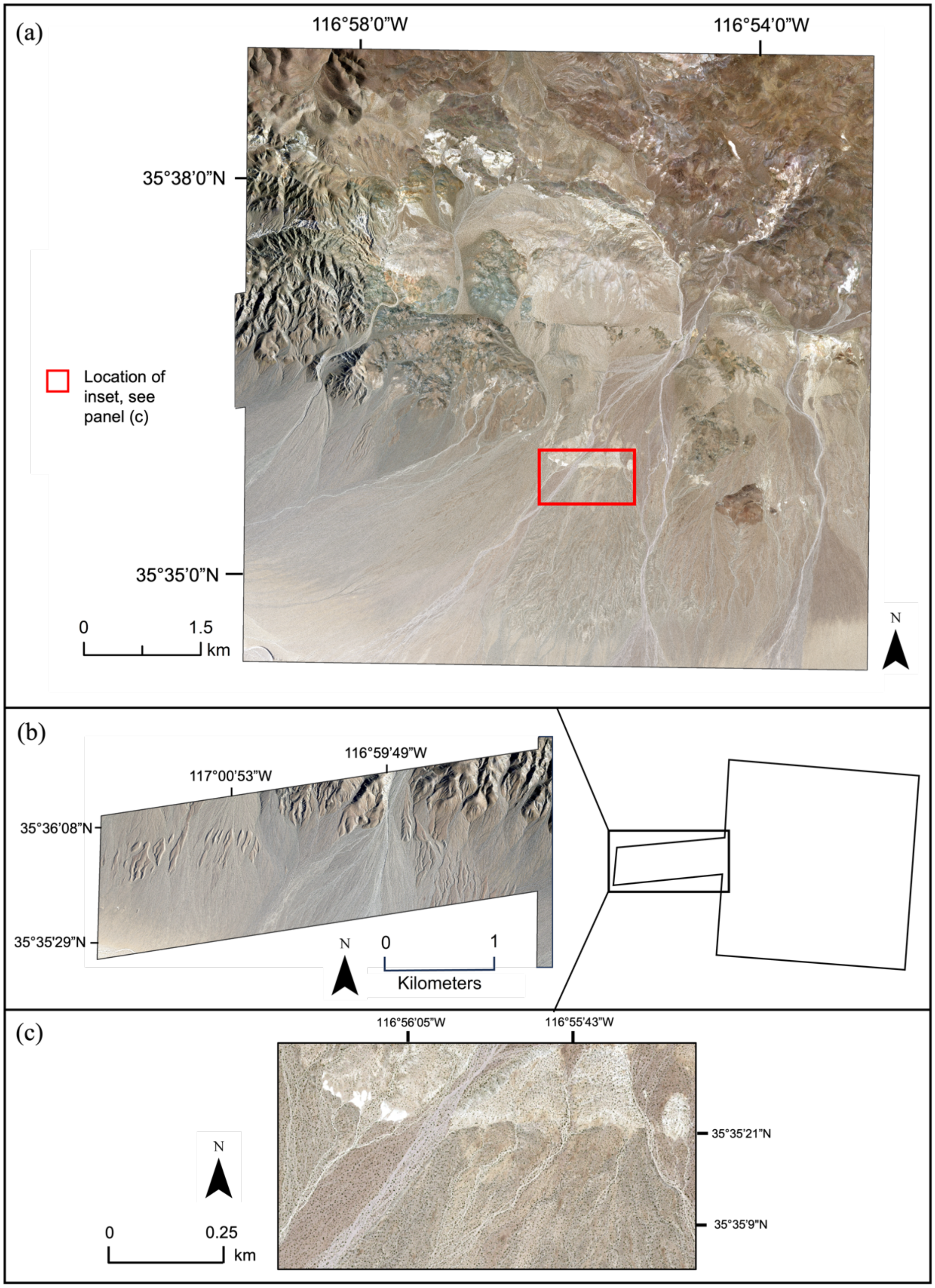

Figure 3-1. (a) Eastern extent of the NAIP imagery of the mapping region; (b) NAIP imagery of the western portion of the mapping region; (c) Example region of NAIP imagery showing different colors and textures displayed in the NAIP imagery used to distinguish different alluvial units.

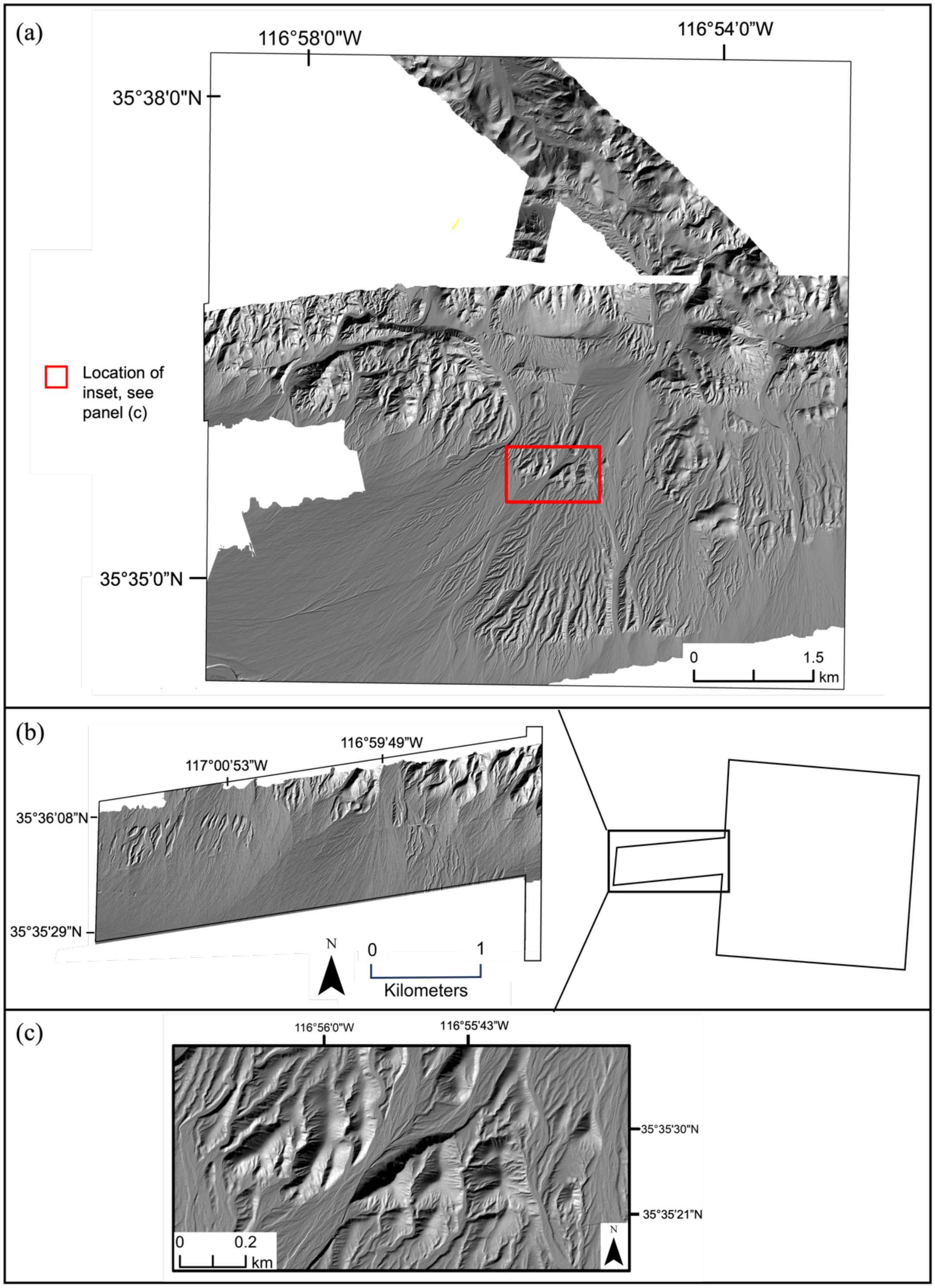

Figure 3-2. (a) Eastern extent of the LiDAR hillshade map used to create the digital map, with a sunlight azimuth of 315° from north and altitude of 25° from the horizon; (b) LiDAR hillshade of the western portion of the mapping region; (c) example region of features highlighted by the LiDAR hillshade.

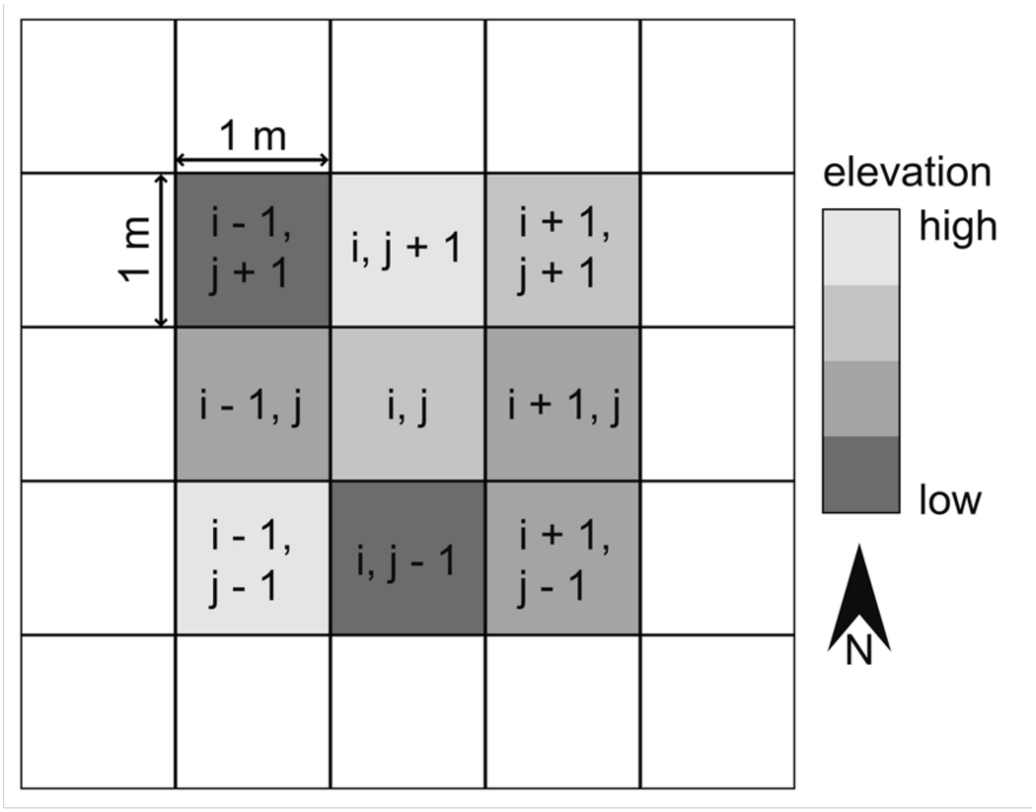

Figure 3-3. Schematic diagram of surface roughness calculation. Calculating the standard deviation of the slope in a 3-m by 3-m window. Each cell is 1-m by 1-m, determined slope values are calculated as the maximum difference between cells in the east-west and north-south directions. The surface roughness map is calculated by taking the standard deviation of all nine surrounding cells and is reported in the center cell (i, j) of each window. *From Frankel et al., 2007.*

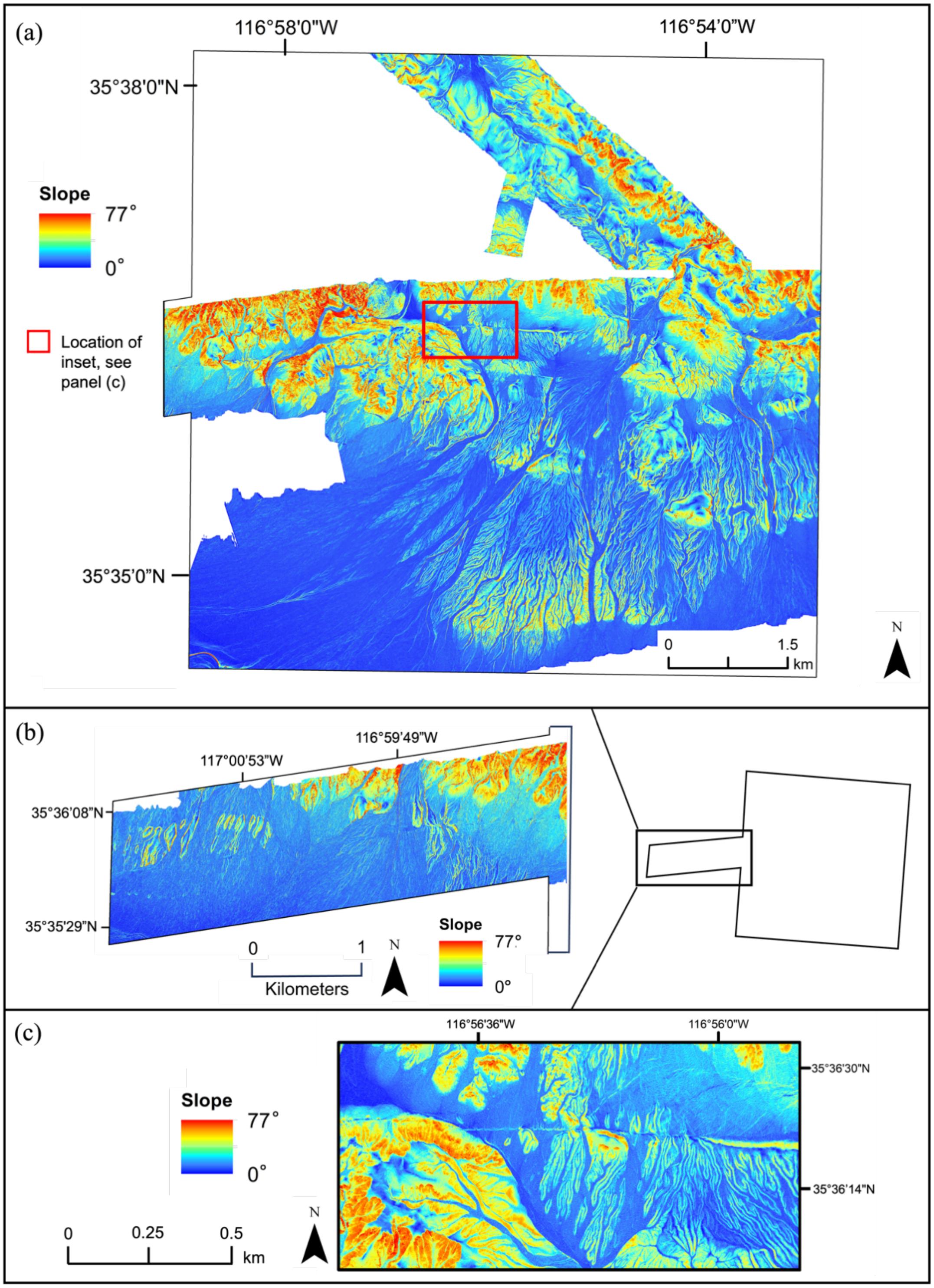

Figure 3-4. (a) Eastern extent of the slope value map derived from the LiDAR digital elevation model. Slope values range from 0.00276467° to 77.3401°; (b) Western extent of the slope value map; (c) Example region the slope map highlighting geologic features (e.g. fault traces, alluvial wash channels highlighted by the slope variations).

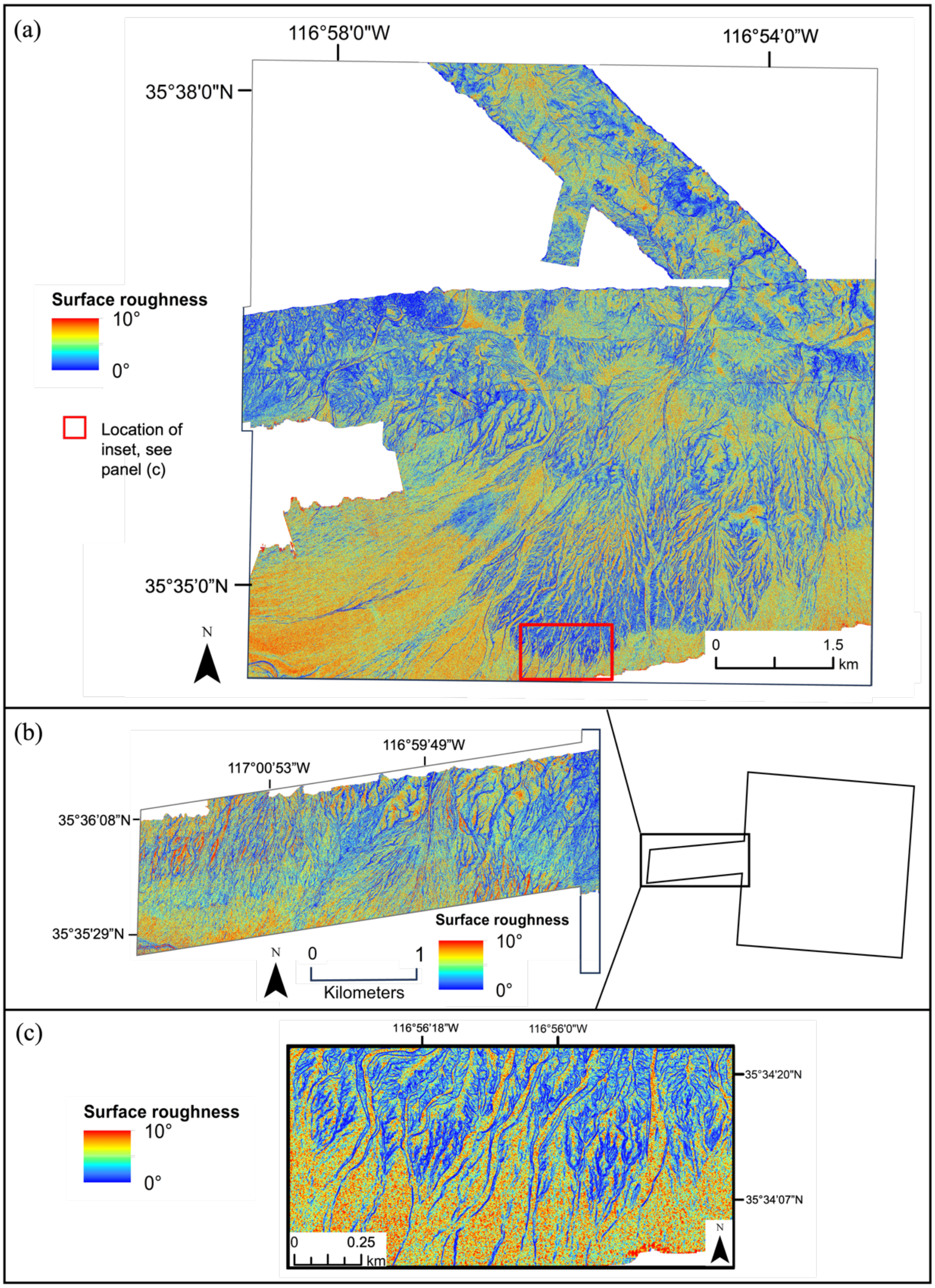

Figure 3-5. (a) Eastern extent of the calculated surface roughness map used to differentiate alluvial units of different ages. Chosen values to display include the surface roughness values from 0° to 10°; (b) western region of the calculated surface roughness map; (c) example region of two different surface ages illuminated by the differences in surface roughness values.

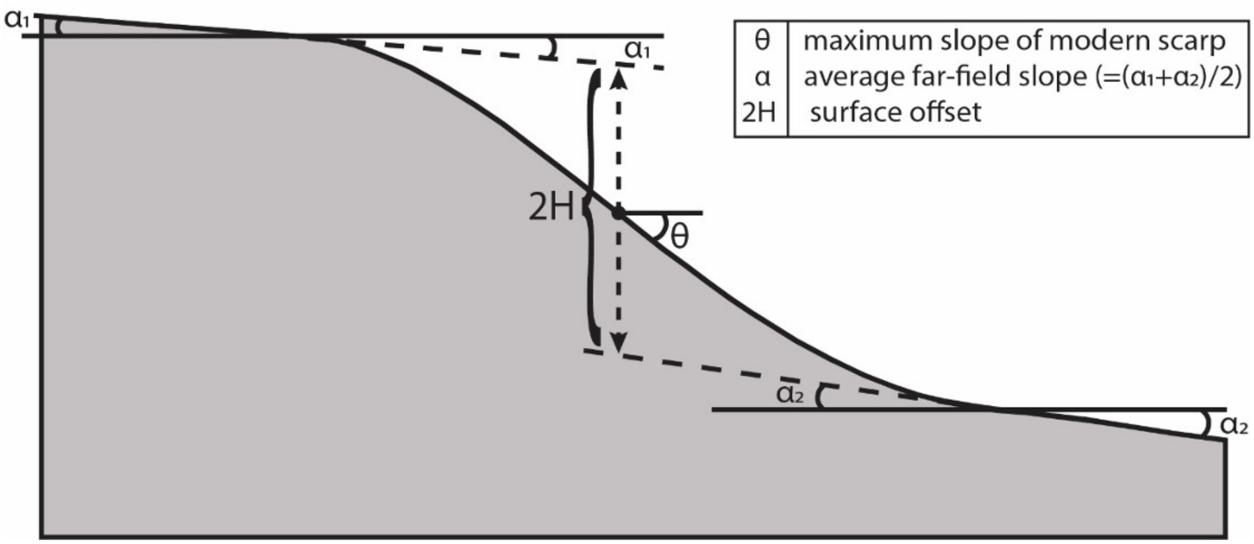

Figure 3-6. Schematic diagram of fault-scarp geometry. The values required for scarp degradation analysis are shown in the diagram; θ: maximum slope of current scarp geometry; α: average far-field slope; 2H: surface offset.

4. RESULTS

4.1. Digital Mapping Product

The mapping product produced from the previously mentioned method is shown in Figure 4-1. The bedrock unit descriptions and locations were adapted from Walker et al. (2002), the shapefiles were further scrutinized and edited to be more precise. Ten different alluvial units of different ages were identified (Qf1-Qf10) and a complex array of fault networks was delineated. The primary mode for differentiation of different alluvial units of different ages was the surface roughness values, NAIP color imagery, and topological relief (Table 4-1). Of the created surface roughness map, the histogram of calculated surface roughness values ranged from 0 to 41.18 degrees, with a mean value of 4.46 and a standard deviation of 1.18. The majority of the surface roughness values are much smaller than the maximum 41.18, this large range of values can be due to the natural topography, but also from data errors in the captured LiDAR field. In order to create the usable map that easily distinguishes the different alluvial units, the symbology of the surface roughness map was edited, the final product excluded the large magnitude outlier values and only included values from 0 - 10 degrees.

Qf1 was the oldest distinguished unit and the highest relief from the surrounding units, the associated surface roughness values are 0-0.65° with an average of 0.46°. In NAIP imagery, Qf2 appears white and tan, with sharp scarps along the incised channels, while Qf2 appears more red in color with more high relief between the raised unit and lower incised channels. Qf2 and Qf3 were originally thought to be of different ages, due to the differences in topographic relief and the observed color discrepancies. Upon further examination, both units have similar surface roughness values of between 0.53-1.94° with respective average of 0.82° and 0.88°, and thus may be of similar age. The differences in relief between the units can be attributed to the southernmost reverse fault's morphological effects on Qf2. Additionally, the color difference in units can possibly be attributed to a difference in the provenance of alluvium from the variety of surrounding bedrock units. Therefore, it was determined that Qf2 and Qf3 may be different compositions but equal in relative age. Qf4 is a unit with moderate relief and surface roughness values between 1.20-3.45°, and an average of 2.17° .Qf5 and Qf6 are very similar in topographic relief, however they differ in surface roughness values with Qf5 and Qf6 having an average surface roughness of 2.74° and 3.41°, respectively. Qf7 and Qf8 are units with low topographic relief that incise the previously mentioned older units Qf1, Qf2, Qf3, and Qf4. These units were divided based on the surface roughness values. Qf7 has values between 1.47-5.77° and an average of 4.08°, and unit Qf8 has values between 3.46-7.84° and an average of 4.69°. Qf9 and Qf10 are the youngest alluvial units in the mapping area. These units are the smallest in area, and are all within incised channels. Unit Qf9 has surface roughness values of 3.26-6.48° and an average of 5.13°, Qf10, the youngest unit, has values between 2.74-9.79° and an average of 6.90°.

Fault traces were primarily delineated using the created LiDAR hillshade and slope map. The observed traces seen on the LiDAR hillshade were linear boundaries that broke the continuity of the smooth hillshade values, on the slope map the fault traces showed as high angle slope values with a large magnitude discrepancies to surrounding slope values (Figure 4-2). The fault traces deemed "certain" were indisputable lineaments seen in both the LiDAR hillshade or the slope map. "Inferred" and minor faults are lineaments that were ambiguous or contained non-significant regional movements. Reverse faults in the mapping region that are certain are denoted by thick, solid lines, whereas the implied reverse faults are dashed, thin lines.

4.1.1. Observed Fault Trends

Within the map region, there are numerous observed fault traces in both the east-west and northwest-southeast trending directions. Overall, 97 independent fault traces were mapped in this region. The overarching characteristics of these fault traces include discontinuous, fragmented segments and complex intersections. Of the mapped faults, 12 are identified as dip-slip and the remaining 85 are strike slip faults, with left-lateral strike slip faulting as the dominant fault type.

The observable dip-slip faults are found within the alluvial fan unit Qf2 in the southern region of the map and across the western portion of the map through Qf1 and Qf7 (Figure 4-3). The identified reverse faults are often in associated conjugate pairs; few identified reverse faults are also components of horst and graben-like structures. To calculate the average attitudes of the reverse faults, three 3-point problems were used to calculate the strike and dip of the three largest reverse faults in the mapping region. These calculations were completed using a 1-m contour map of the mapping region. The average calculated strike was 083 and the average dip was 9.25°. In the southern portion of the map a large horst structure affects the alluvial unit Qf2 (Figure 4-2a), and graben structures in the western reverse faults. All the observed reverse faults have an east-west strike, the southern scarp terraces have heights up to 11-m of vertical relief, while the western scarps have smaller offsets up to 4-m of vertical relief.

In the mapped region, both the Garlock fault and the Brown mountain fault become fragmented as they intersect. The dominant observed trend in the fault interaction is that the northwest-southeast striking segments of the Brown Mountain fault are truncated by the east-west striking fragments of the Garlock fault (Figure 4-4). This trend is not universal to all faults, there are observed northwest-southeast striking faults truncating east-west fault traces. The observed truncations were quantified: (1) 29 northwest-southeast faults are truncated by east-west striking faults; and (2) 11 east-west striking faults are truncated by northwest-southeast striking faults. A rose diagram showing the orientations of the identified strike-slip faults in the mapping region can be seen in Figure 4-17. The dominant trend of these structures is east-west trending, with an average strike of 099. Of the faults not accounted for in those numbers, they were not counted due to ambiguity either in fault certainty or association with the larger east-west Garlock and northwest-southeast Brown Mountain systems. Additionally, in the western segment of the map section northeast-southwest striking R-shear fault structures stem from the left lateral strike-slip faults.

4.2. Lateral Offset Measurements

A select few of the digitally mapped alluvial units have very apparent left-lateral offsets that are identified on the map product (Figure 4-15; locations #1-7). Locations #1 and #2 are lateral movements within the alluvial unit Qf1, the oldest identified Quaternary unit. Locations #3 and #4 are identified offsets in the alluvial unit Qf2, the second oldest Quaternary unit. Due to the relatively older ages of these two units, the larger relief of the alluvial fans allows for easier reconciliation of pre-fault geometries because the geomorphic features stand out from the surrounding wash. In locations #1 and #2 the apparent displacement in both locations is of similar magnitude and after being restored to pre-faulting geometries, the measured offsets are 198-203 meters and 175-184 meters respectively. The measured displacements at locations #3 and #4 are 157-162 meters, and 178-182 meters. Detailed maps of the offset measurements can be seen in Figure 4-16.

Of the younger units, Qf1r1D and Qf10, the youngest and second-youngest units, both had measurable left-lateral offsets. Location #5 is within the unit Qf10 in the central area of the mapped region. This region has many fault intersections, both east-west and northwest-southeast striking faults intersecting with one another. Due to the characteristic of this region, it is difficult to attribute the measured offset to a single fault or group of faults, which makes the location #5 measurements are less reliable for slip-rate calculations. The measured offset at this location was 117-122 meters.

In the western portion of the mapped region, two offsets were identified which are isolated from the northwest-southeast striking faults, and appear to be only affected by the left-lateral segments of the mapped faults. Location #6 is a left-lateral offset of the youngest alluvial unit, Qf1r1D. Restoring this alluvial unit was more ambiguous than the older units due to the similarity in both surface roughness and shape of the unit to the surrounding features, which in turn, yielded a greater error margin in total magnitude of offset. The measured displacement in location #5 is 116-164 meters. Location #7 is a truncation of a wash channel in the unit Qf5 along the east-west fault trace of the Garlock fault. The measured offset of location #7 is 111-116 meters. Both of the locations, #6 and #7, have a higher significance to the Garlock fault slip rate due to the distance from the Brown Mountain fault intersection and its associated fault segments' behavior. The identified locations with measured displacements can be seen in Table 4-2.

4.3. Scarp Degradation Analysis

In the map region, fourteen profiles were extracted from the LiDAR point cloud to determine the most recent movements along either the fault traces or terrace risers of alluvial units using the previously mentioned method of scarp degradation analysis (Figure 4-5). The selected profiles were chosen to satisfy the requirements of being a smooth contour with one slope value and no jagged regions of varying slope or gully features. Detailed LiDAR hillshade maps of each profile can be seen in Figure 4-6. From the applied Python model, each profile analysis yielded both the vertical displacement (2H) and total degradation (κt) for either single event, multi-event, or both. From the given total degradation value, the aforementioned κ value was used to calculate the timing of the most recent movement along the extracted profiles.

4.3.1. Dip-Slip Profiles and Calculated Vertical Slip Rate

The extracted profiles that correlate to dip-slip faults are useful in determining the timing of the latest movements along the regional reverse faults. The profiles Qf3t1E, Qf1r2F, Qf1r3F, and Q1gF are scarps along reverse faults. Qf3t1E is located in the southern portion of the map and has an offset height of 1.59 ± 0.03 m, a total degradation value of 20.4 ± 1.2 m^2 and age of 78 ± 30 kyr when modeled as a single rupture event, and values of 46.5 ± 3.3 m^2 and 179 ± 71 kyr when modeled as a steady state slip. Profiles Qf1r2F, Qf1r3F, and Q1gF are located in the western region of the map in location F. Profile Qf1r2F has a vertical offset magnitude of 1.75 ± 0.05 m, a total degradation value of 13.1 ± 1.5 m^2 and age of 51 ± 22 kyr when analyzed under single event uplift and respective values of 30 ± 4.3 m^2 and 118 ± 54 kyr under steady state uplift analysis. Profile Qf1r3F has a vertical offset value of 1.25 ± 0.03 m, a total degradation of 1.2 ± 0.4 m^2, and yielded an age of 5.0 ± 3.0 kyr under single event analysis and magnitudes of 3.2 ± 0.4 m^2 and 12.5 ± 5.5 kyr under steady state analysis. Profile Q1gF has a vertical offset of 0.39 ± 0.02 m, total degradation of 1.1 ± 0.3 m^2 , and calculated age of 4.5 ± 2.5 kyr under single event conditions and values of 2.4 ± 0.8 m^2 and 10.0 ± 6.0 kyr under steady state conditions. Additionally, the extracted profiles Qf1r3F and Qf1r1D have upper and lower slopes that are not parallel, suggesting the lower alluvial surfaces were modified in some way. This makes these profiles unsuitable for scarp degradation analysis, but still viable to use still for uplift magnitude. The results of the scarp degradation analysis that correlate to dip-slip profiles can be seen in Table 4-5. Using the LiDAR point cloud, the offset height was extracted for each profile (the previously mentioned value, H). Using the extracted offset heights and calculated ages of movement along these scarps, the average vertical slip rate was calculated to be 0.15 ± 0.12 mm/yr (Table 4-7).

4.3.2. Left-Lateral Profile Analysis

The extracted data from the profiles that correlate to left-lateral fault movement can be found in Table 4-3. To describe the different profiles, they are categorized by identifying the "upper" alluvial unit, which is the topographically higher unit of the scarp, and the "lower" alluvial unit, which is the topographically lower unit at the bottom of the scarp. This is done to identify the timing that the extracted profile will distinguish- not all profiles will give the timing of the latest movement along the Garlock fault or correspond to the lateral measurements (see Table 4-4).

The three locations in the eastern portion of the geologic map include locations A, B, and E. Location A includes profiles Qf1r1A, Qf7rb2A, and Qf7rb3A. Both Qf7rb2A and Qf7rb3A run across Qf7 for both the upper and lower alluvial units. Profile Qf1r1A runs from the upper unit of Qf1 to the lower unit of Qf7. Location B includes a terrace riser profile, Qf25r2B, which plots across the upper unit of Qf2, and the lower unit Qf4. Location E includes the profile Qf3t1E, which is a scarp across the southernmost reverse fault in the mapping region across the alluvial unit Qf2. In the western region of the map, locations C, D, and F include the majority of extracted scarp profiles. Location C includes Qf4r1C and Qf4r2C. Both of these profiles have an upper and lower alluvial unit of Qf5. Location D includes profiles Qf1r1D, Qf1r4D, Qf4r1C, Qf4r2C, Qf17r1D, Qf17r2D, and Qf17r3D. Profiles Qf1r1D and Qf1r4D have the same upper and lower alluvial unit, Qf1. Profiles qf1Q4r2C and qf1Q4r2C have Qf1 as the upper unit, and

Qf5 as the lower unit. Profiles Qf17r1D, Qf17r2D, and Qf17r3D have an upper unit of Qf1 and a lower unit of Qf7. Location F includes Qf1r2F, Qf1r3F, and Q1gF; all of which have an upper unit and lower unit of Qf1.

The diffusion analysis performed yielded the following results. Profile Qf1r1A has an offset height of 2.29 ± 0.04 m, a total degradation value of 5.1 ± 0.4 m^2 , and calculated age of 19.6 ± 7.8 kyr under single event uplift conditions. Analysis on profile Qf7rb2A generated an offset magnitude of 0.22 m, a total degradation value of 0.6 m^2 , and age of 2.23 ± 0.8 kyr by single event uplift analysis. Profile Qf7rb3A has an offset height of 0.55 m, a total degradation value of 1.5 m^2 , and yielded an age of 5.6 ± 1.9 kyr analyzed under single even uplift. The vertical offset magnitude for profile Qf25r2B was 3.2 m, the total degradation value was 21.7 m^2 , and the calculated age was 81.4 ± 27.1 kyr under single event uplift analysis. Profile Qf1r1D yielded an offset magnitude of 4.19 ± 0.09 m, however was not used for scarp degradation analyses because the geometry of the scarp was not viable. Profile Qf1r4D has an offset magnitude of 2.01 ± 0.06 m, a total degradation value of 11.3 ± 1.7 m^2 , and calculated age of 44.5 ± 20.5 kyr for single event uplift modeling, and values of 25.5 ± 4.2 m^2 and 101 ± 47.6 kyr for steady state uplift modeling. The offset height for profile Qf14r2D was 0.88 ± 0.03 m, the total degradation amount was 2.4 ± 0.5 m^2 , and the age was 9.6 ± 4.9 kyr under single state analysis. Profile Qf17r1D yielded an offset height of 3.93 ± 0.04 m, a total degradation of 12.2 ± 0.6 m^2 , and an age of 46.5 ± 17.5 kyr under single event analysis. Profile Qf17r2D has a vertical offset of 1.65 ± 0.05 m, a total degradation value of 3.9 ± 0.6 m^2 , and yielded an age of 15.4 ± 7.1 kyr for single event modeling. Finally, profile Qf17r3D has a vertical offset of 1.46 ± 0.03 m, a total degradation value of 1.0 m^2 , and an age of 3.8 ± 1.3 kyr under single event analysis.

4.4. Lateral Slip Rate

From the previous analyses of offset measurements and age calculations, the slip rate along the east-west fault segments were calculated in millimeters per year of offset. From the analyzed scarp profiles, Qf3t1E, Qf1r2F, Qf1r3F, and Q1gF were not used for the slip rate calculations. As previously mentioned, these profiles are dip-slip scarps, and therefore are unable to be used to calculate the lateral offset rates. From the extracted profiles, the profiles that correspond to the lateral movements were selected for the calculations (i.e. contain the corresponding alluvial unit(s) in the lateral measurement). The scarp profiles that corresponded to these qualifiers are Qf1r1A, Qf25r2B, Qf1r1D, Qf1r4D, Qf4r1C, Qf4r2C, Qf17r1D, andQf17r2D. The lateral offset measurements at locations 4 and 5 were also not used in the slip rate calculations. These lateral measurements did not correlate to analyzed scarp profile locations, and could not be correlated to a scarp profile location without significant error. Figure 4-18 shows the locations of each measurement and whether the results were used as a single strand slip rate, or if they were summed together as multiple branches of the larger fault strand. The results of the slip-rate calculations can be seen in Table 4-8. The average slip rate along the segments of the Garlock fault within the geologic map extent is 11.1 ± 6.7 mm/yr.

GEOLOGIC MAP OF THE INTERSECTION BETWEEN THE GARLOCK FAULT AND BROWN MOUNTAIN FAULT

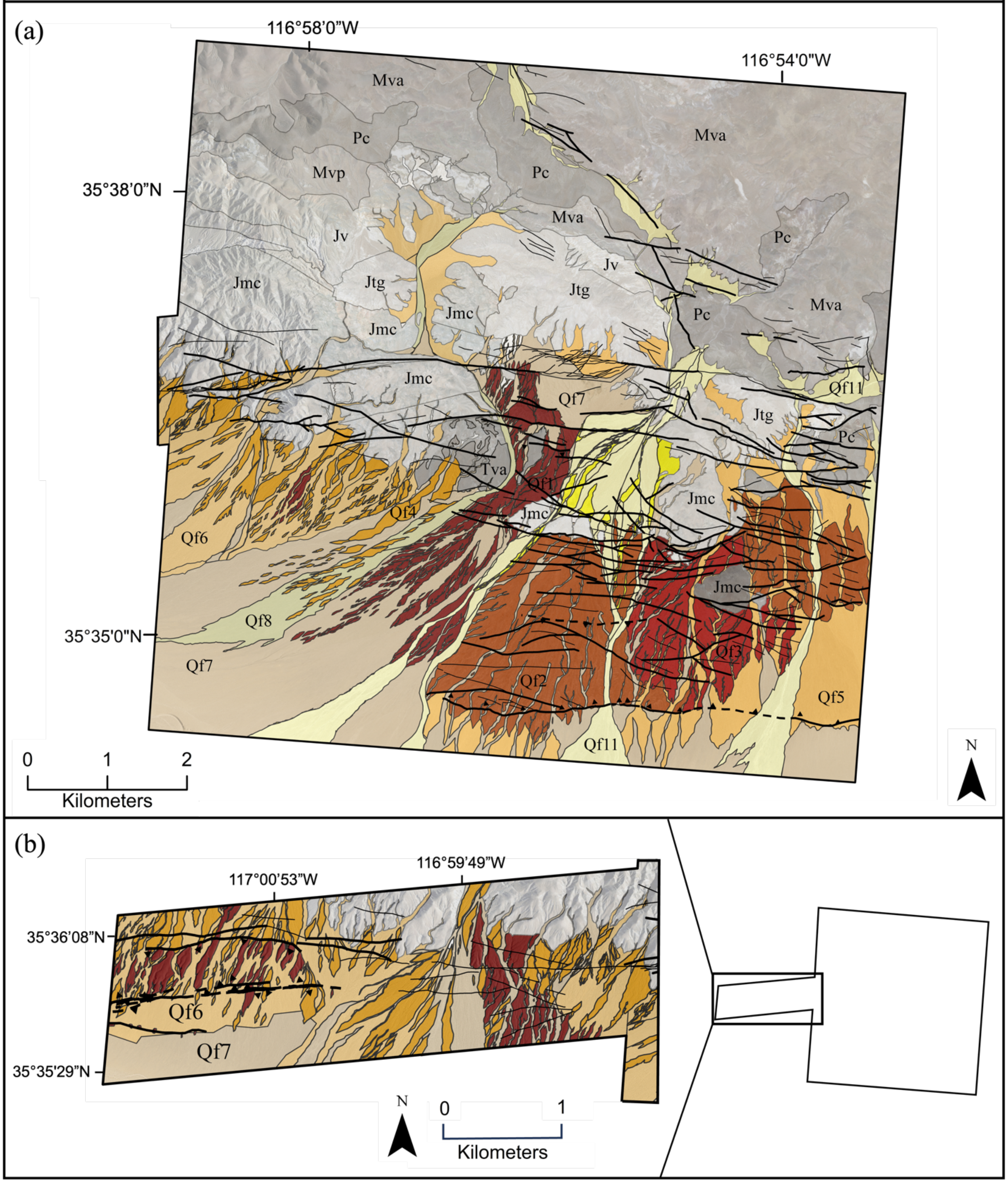

MAP UNITS

ALLUVIAL FAN DEPOSITS

Qf10	**Youngest alluvial fan deposit**
Qf9	**Young alluvial fan deposit**
Qf8	**Intermediate alluvial fan deposit**
Qf7	**Intermediate alluvial fan deposit**
Qf6	**Intermediate alluvial fan deposit**
Qf5	**Intermediate alluvial fan deposit**
Qf4	**Old alluvial fan deposit**
Qf3 Qf2	**Old alluvial fan deposits of the same age but different composition**
Qf1	**Oldest alluvial fan deposit**

BEDROCK UNITS [1]

TERTIARY UNITS

Tva	**Tertiary volcanic andesite**
Pc	**Tertiary Pliocene sedimentary fanglomerate**
Mvp	**Tertiary Miocene volcanic pyroclastic**
Mva	**Tertiary Miocene volcanic andesite**

JURASSIC UNITS

Jmc	**Upper Jurassic igneous mixed complex**
Jv	**Late Jurassic metamorphic metavolcanic**
Jtd	**Late Jurassic igneous tectonized granitoid**
Jd	**Late Jurassic igneous porphyritic diorite**

[1] Bedrock units obtained and modified from *Walker et al., 2002.*

MAP KEY

FAULT TRACES

━━	**Strike-slip fault, certain**
——	**Strike-slip fault, minor or inferred**
▲▲	**Reverse fault, certain**
-▲-▲-	**Reverse fault, inferred**

Figure 4-1. Geologic map of the intersection between the Garlock fault and Brown Mountain fault- broken into two segments (a) the eastern section of the mapping area and (b) the eastern segment of the region.

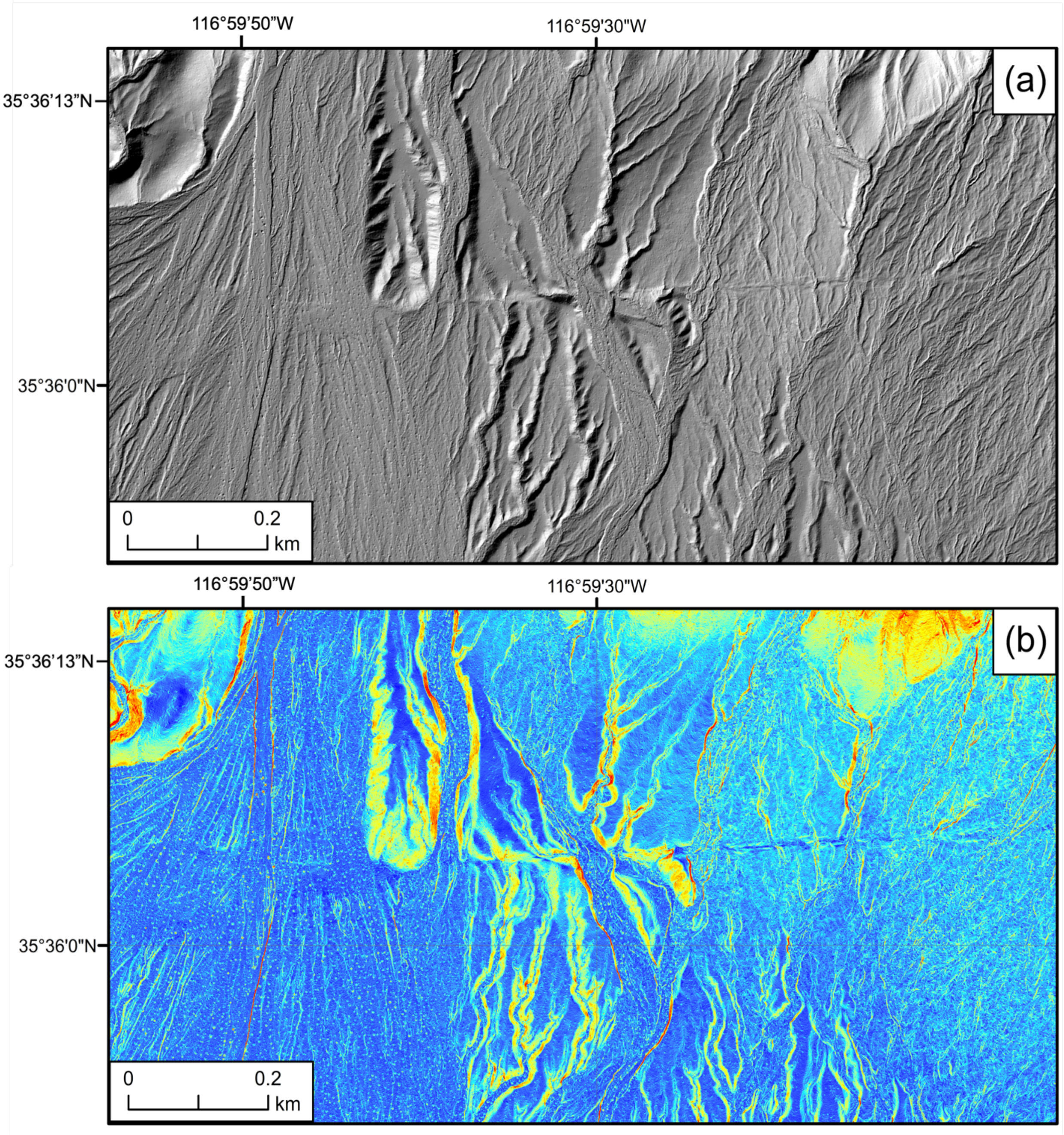

Figure 4-2. Example of the same fault trace in the western portion of the map on the (a) LiDAR hillshade, and (b) slope map.

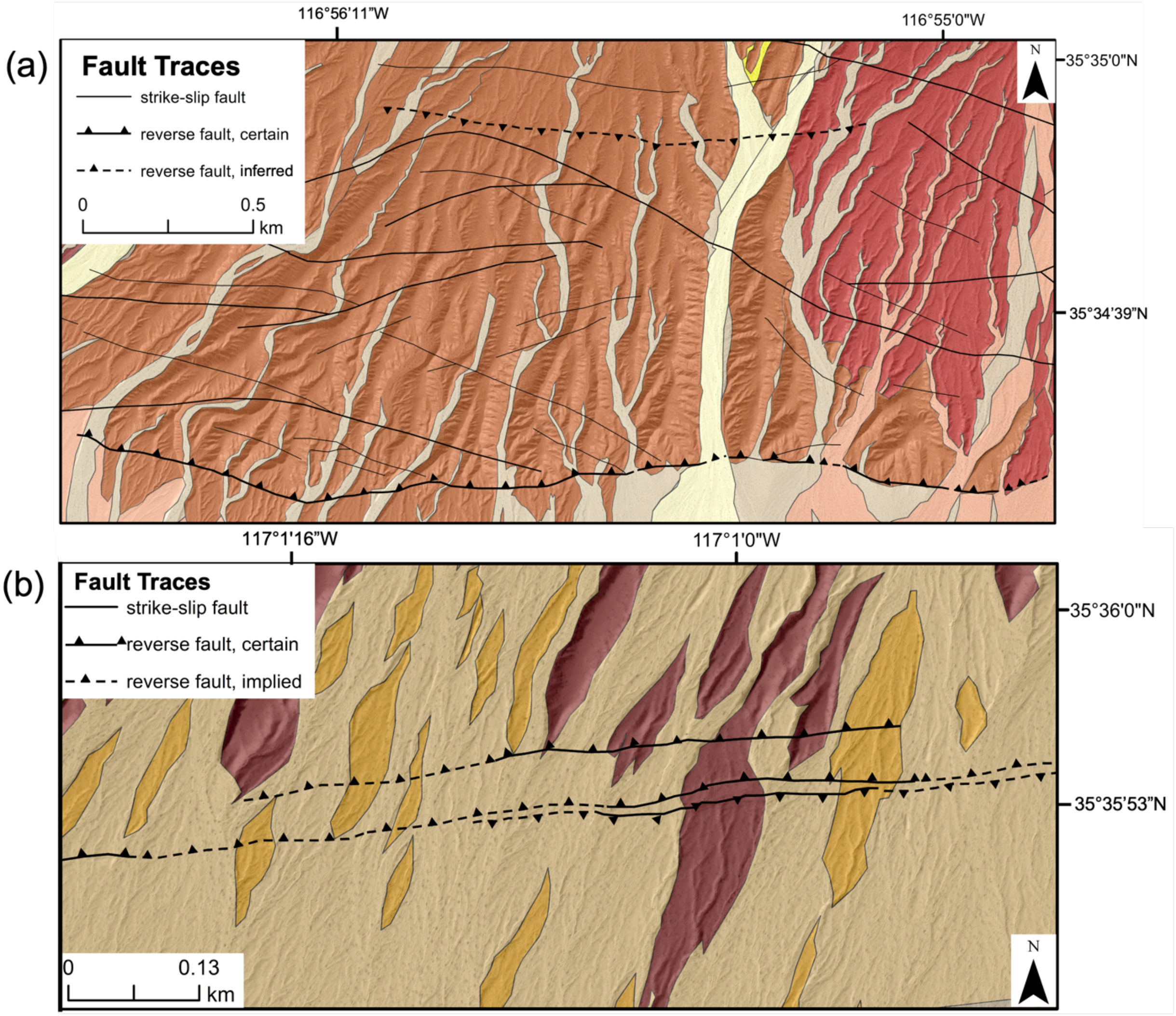

Figure 4-3. Reverse faults within the geologic map extent. (a) within the southern map extent, a large reverse fault and a northern implied reverse fault. These structures create a horst structure in the southern map area in the alluvial unit Qf2. (b) within the western map extent, two reverse faults create a graben structure in the unit Qf1.

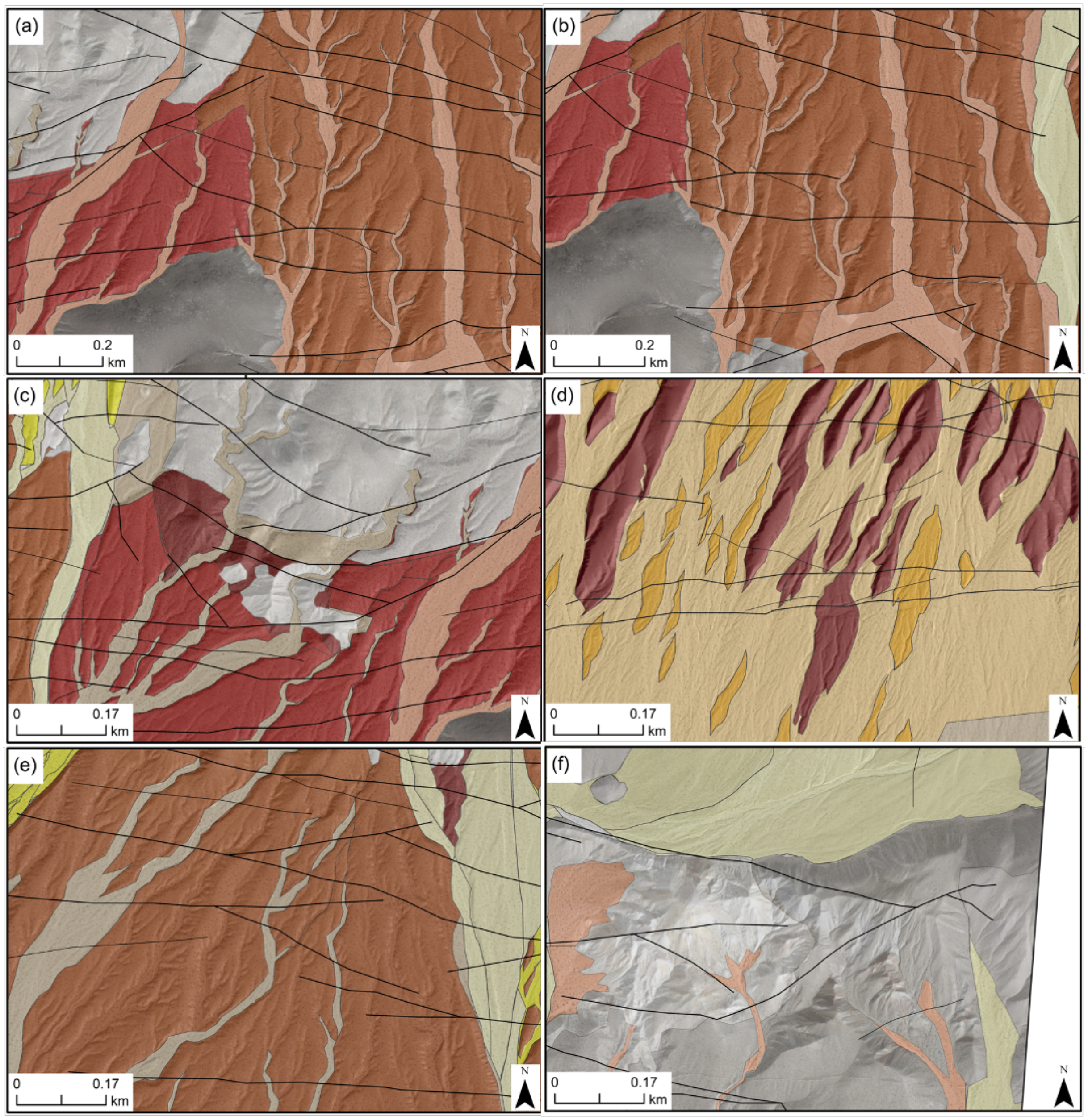

Figure 4-4. Examples of east-west striking, Garlock-associated faults truncating north-northeast striking Brown Mountain-associated faults. Examples (a), (b), and (c) are in the southeastern section of the map; (d) is in the western portion of the map; (e) is in the central portion of the map; and (f) is in the central east portion of the map region.

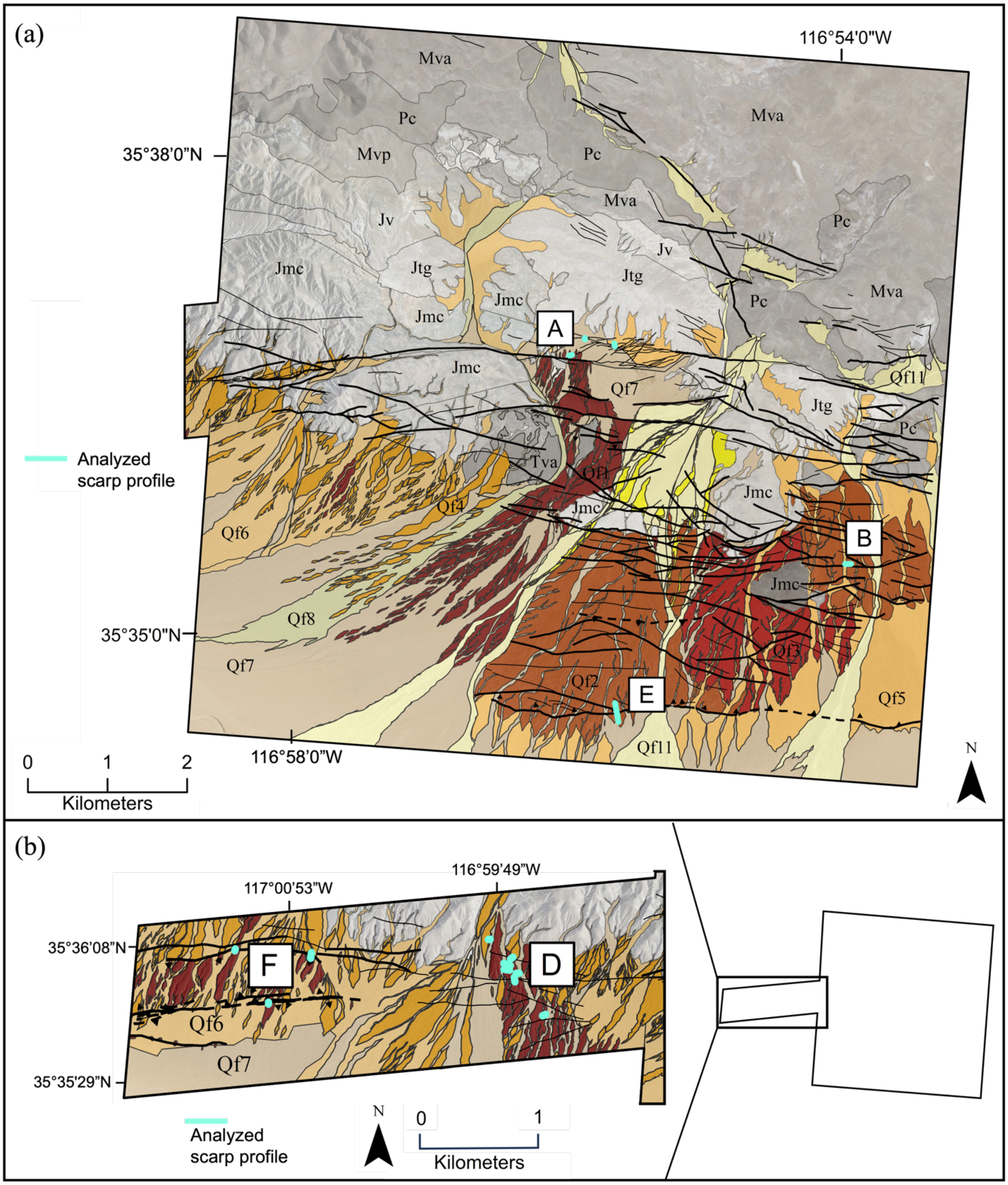

Figure 4-5. Geologic map with analyzed scarp profiles. Generalized locations indicated for groupings of analyzed scarp profiles (Locations A-F). See Table 4-3 and Table 4-5 for individual profile data. See Figure 4-6 for LiDAR hillshade maps of each location (A-F) and associated profiles.

(a) Location A

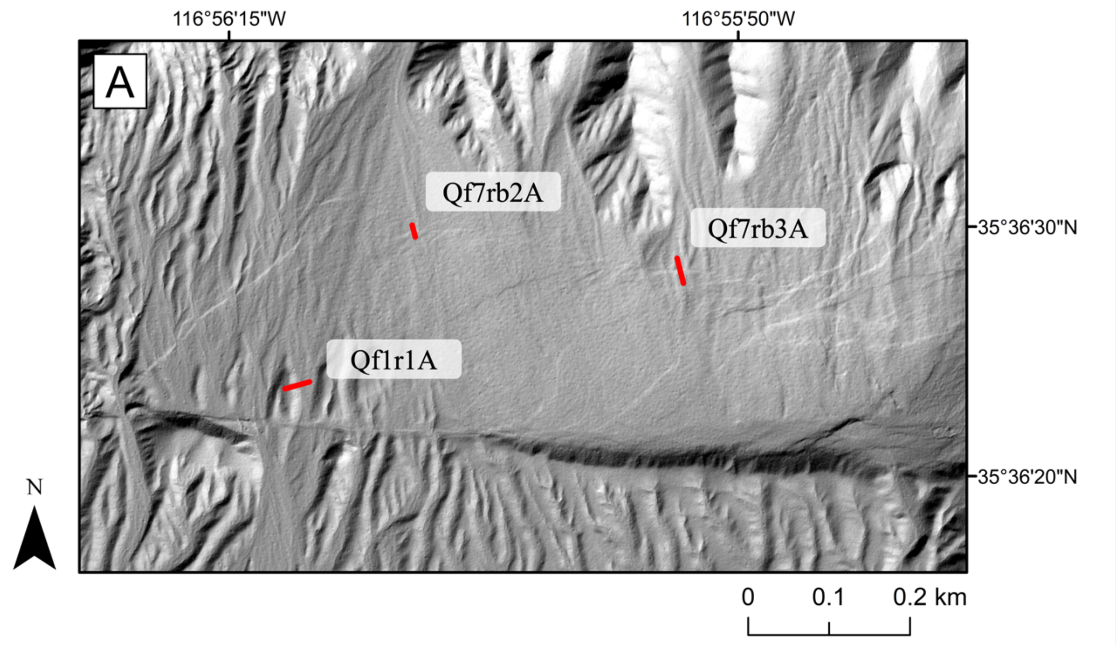

(b) Location B

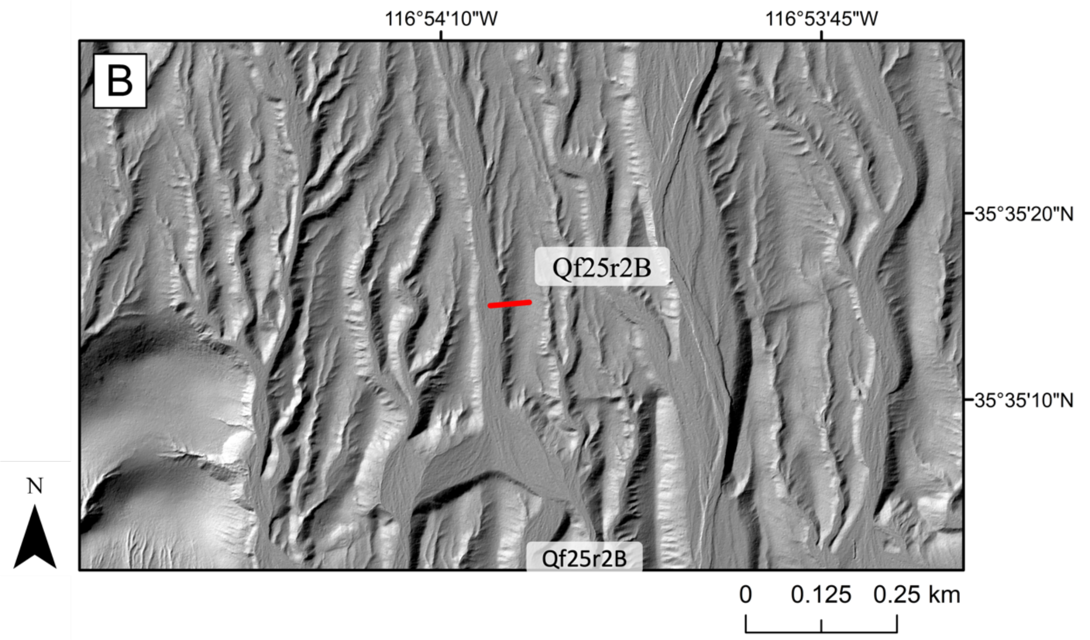

(c)

Location D

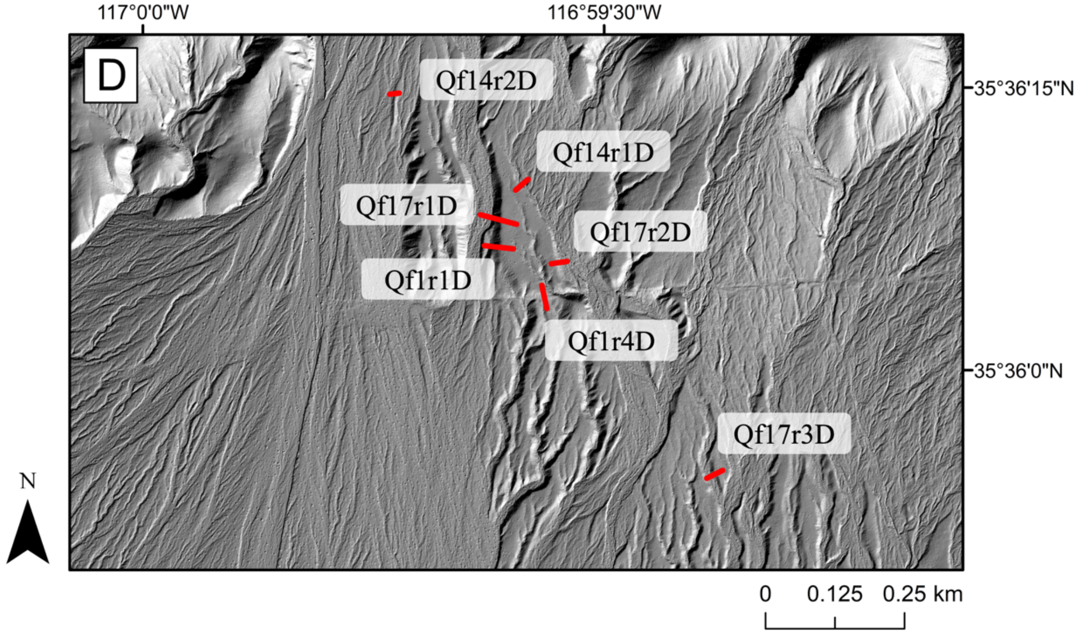

(d)

Location E

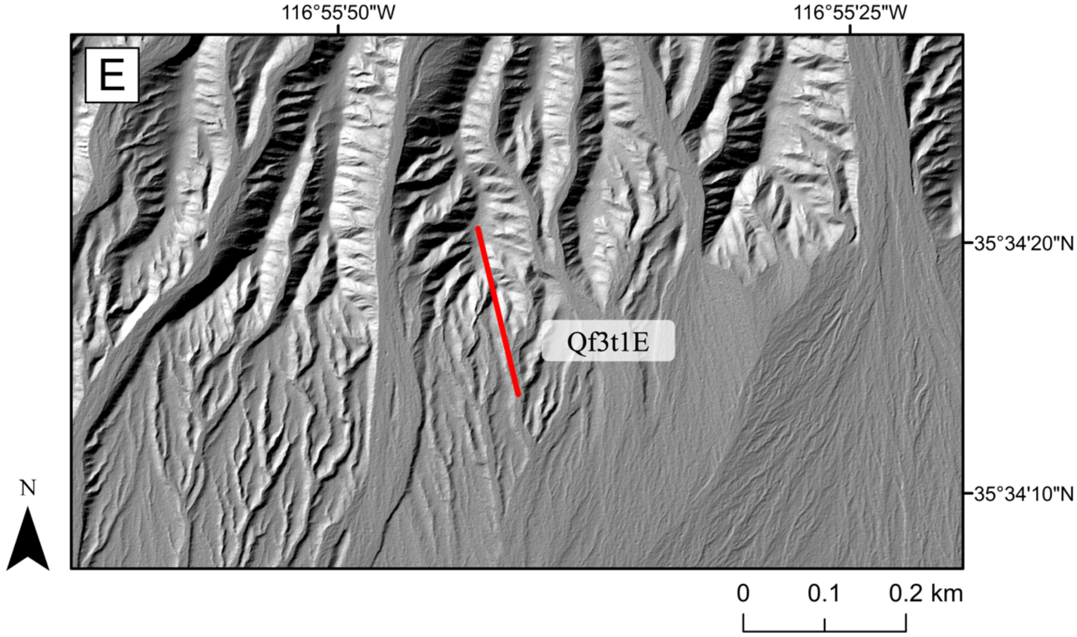

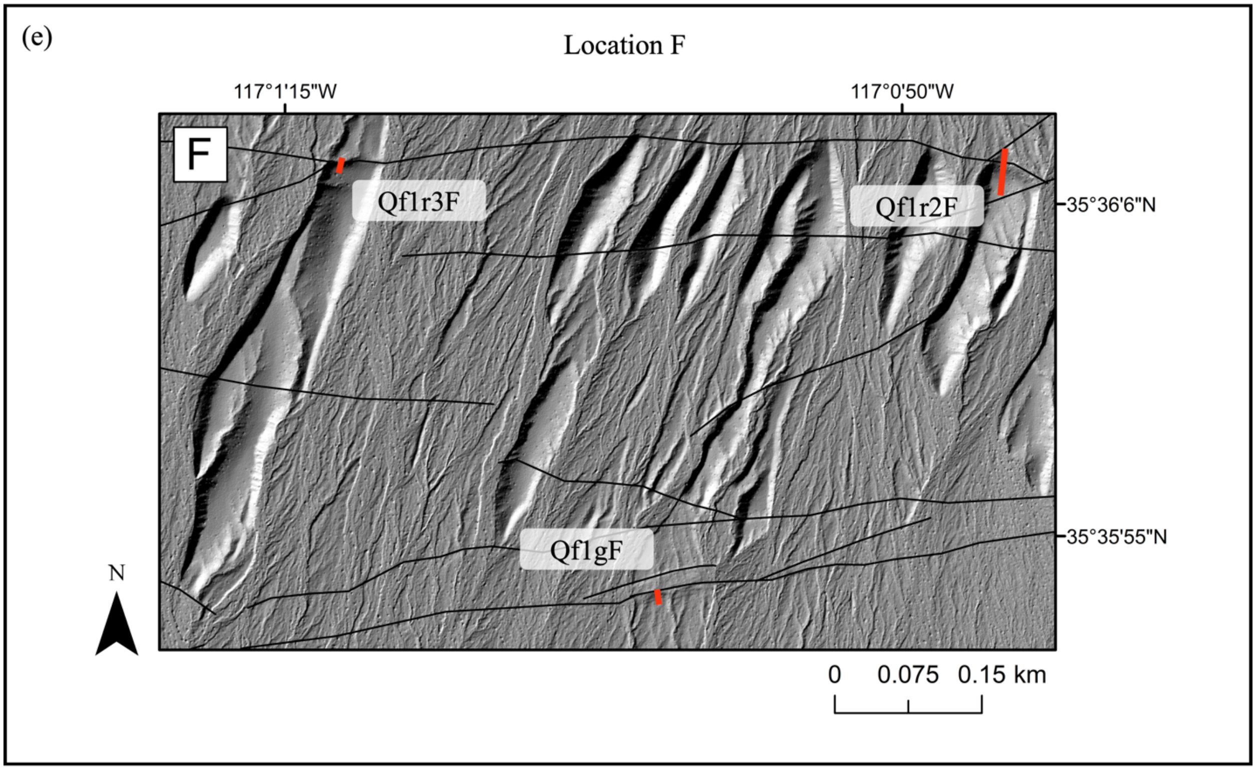

Figure 4-6. LiDAR hillshade maps of analyzed scarp profiles, profiles are highlighted in red and labeled with the associated profile name: (a) Location A; (b) Location B; (c) Location D; (d) Location E; (e) Location F. See Figures 4-7 through 4-14 for individual extracted profile shapes.

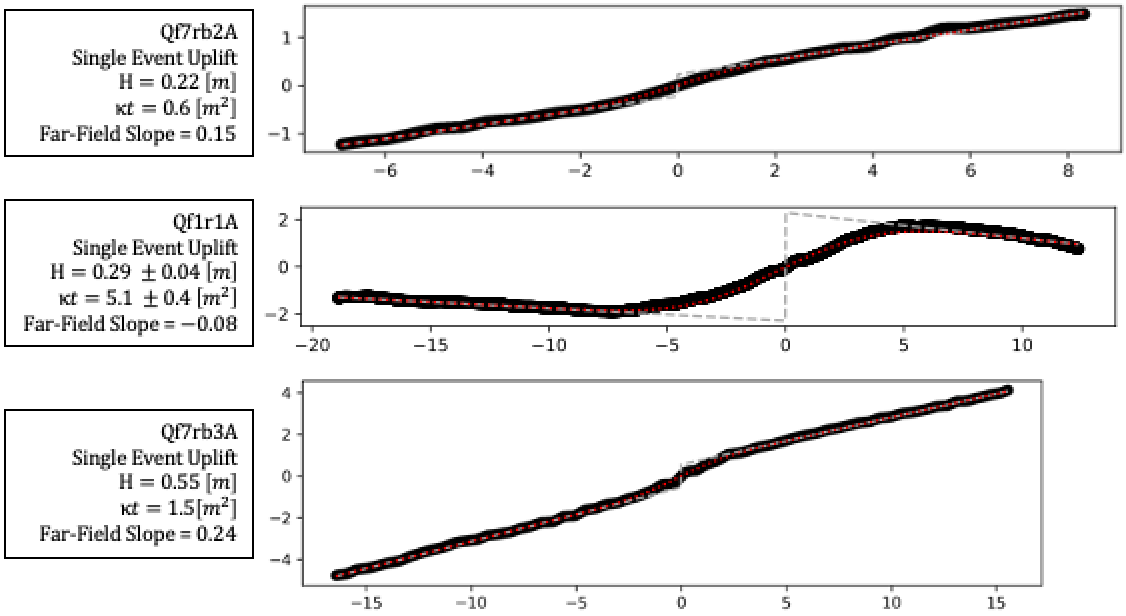

Figure 4-7. Extracted scarp profiles from map location A: (1) Qf7rb2A, (2) Qf1r1A, (3) Qf7rb3A. All are analyzed under single event uplift conditions.

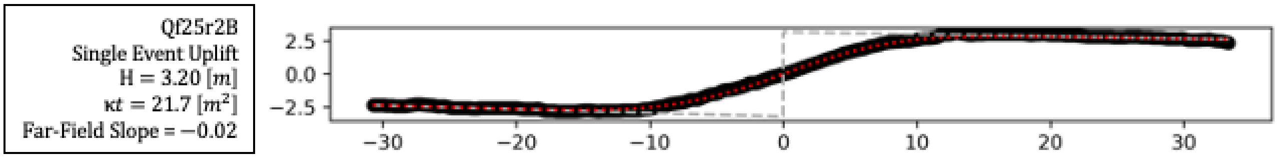

Figure 4-8. Extracted scarp profile from map location B: (1) Qf25r2B. This profile was analyzed under single event uplift conditions.

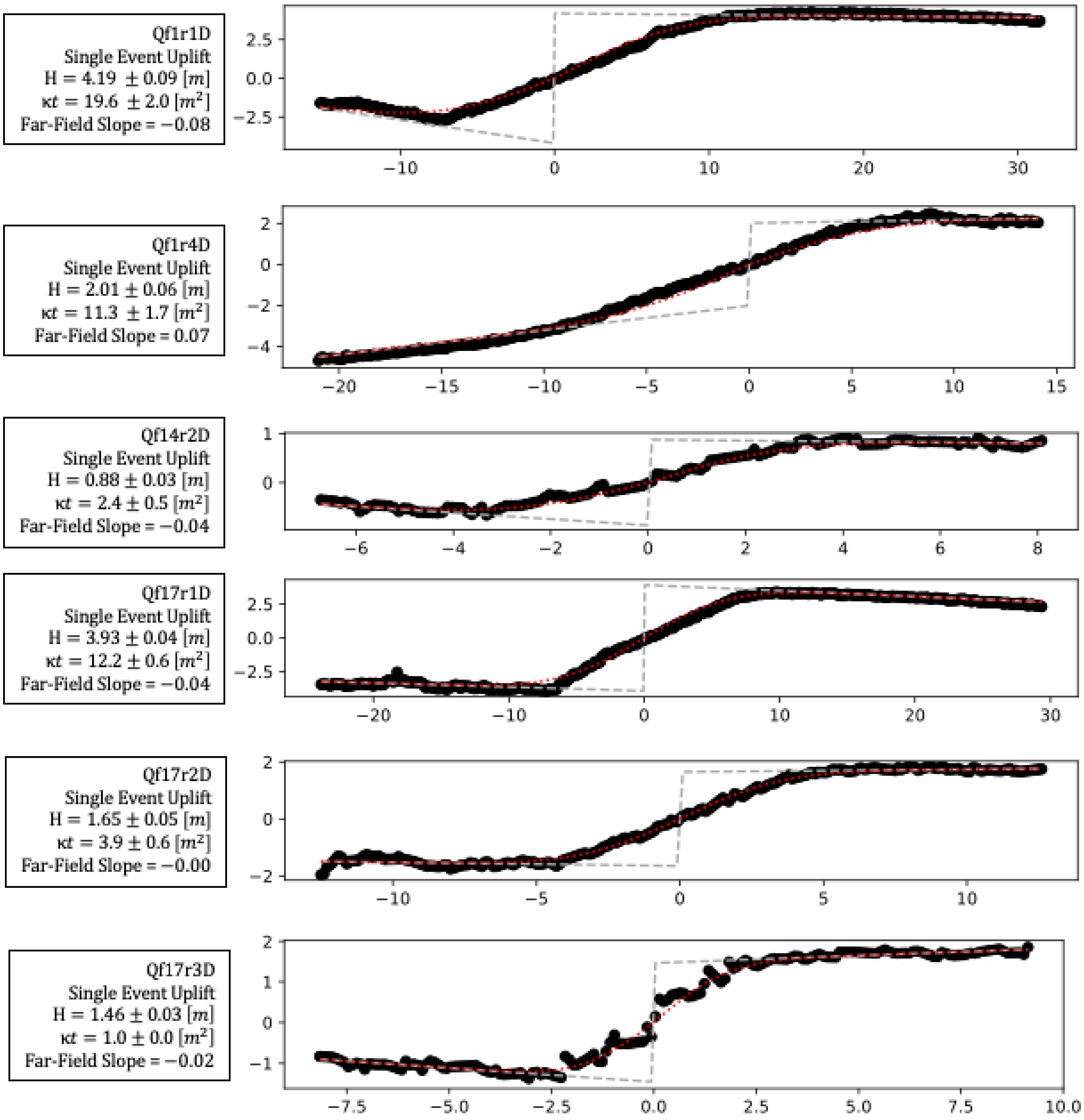

Figure 4-9. Extracted scarp profiles from map location D, analyzed under single event uplift conditions: (1) Qf1r4D, (2) Qf14r2D, (3) Qf17r1D, (4) Qf17r2D, (5) Qf17r3D.

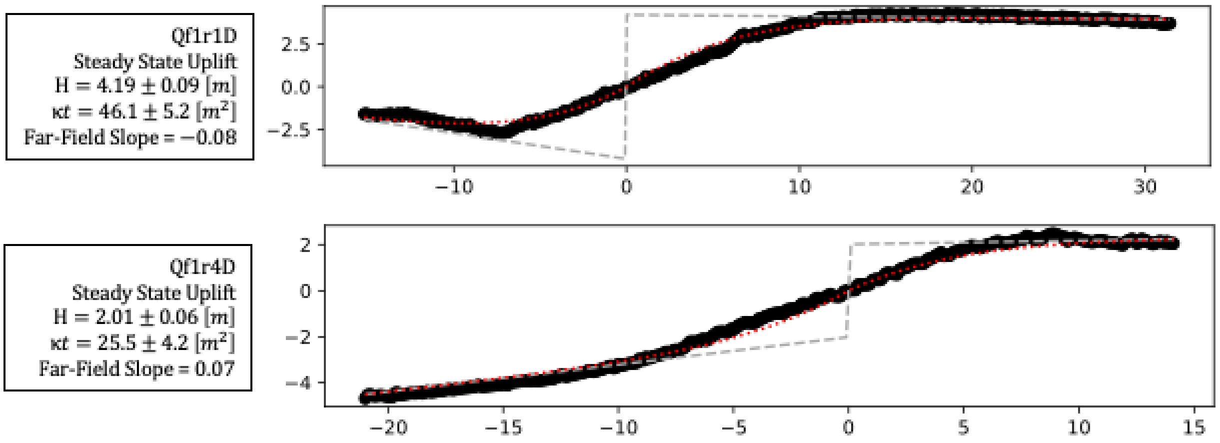

Figure 4-10. Extracted scarp profiles from map location D, analyzed under steady state uplift conditions: (1) Qf1r1D, (2) Qf1r4D.

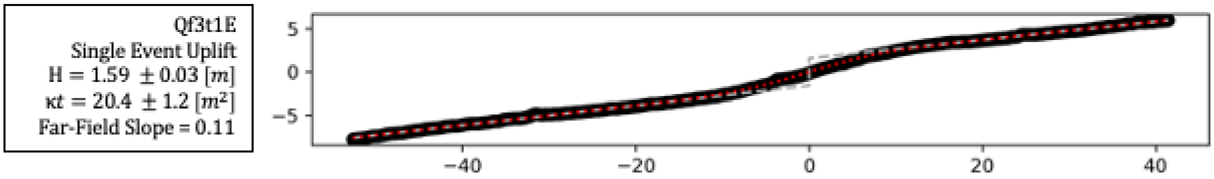

Figure 4-11. Extracted scarp profile from map location E, analyzed under single event uplift conditions: (1) Qf3t1E.

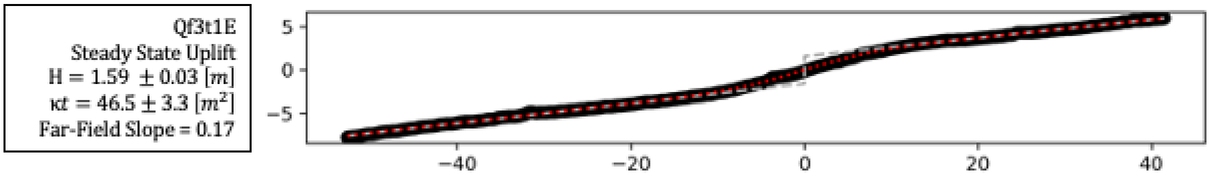

Figure 4-12. Extracted scarp profile from map location E, analyzed under steady state uplift conditions: (1) Qf3t1E.

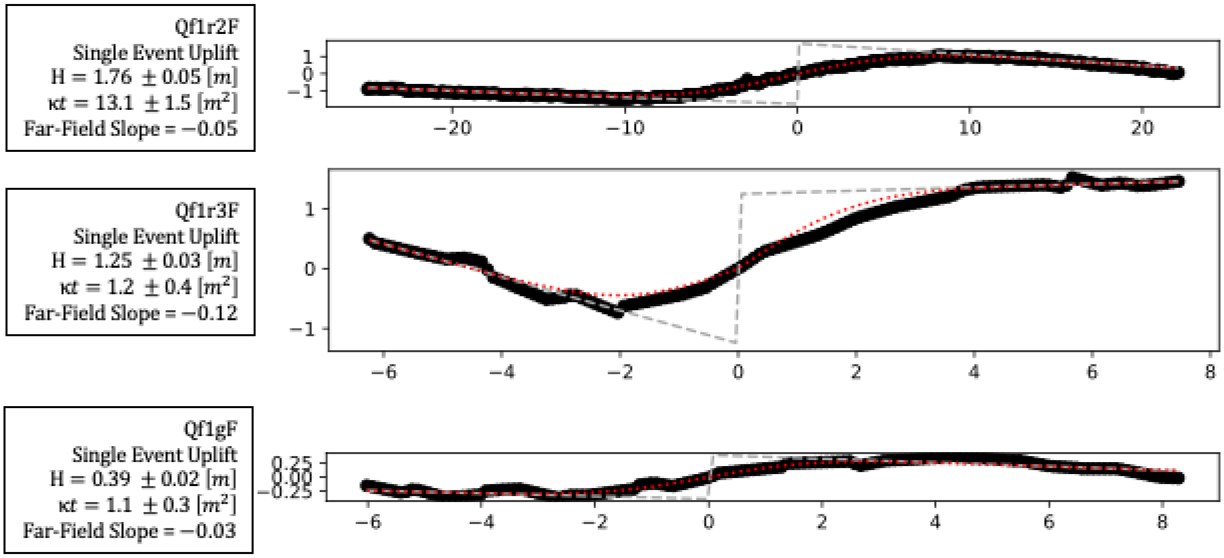

Figure 4-13. Extracted scarp profile from map location F, analyzed under single event uplift conditions: (1) Qf1r2F, (2) Qf1r3F, (3) Q1gF.

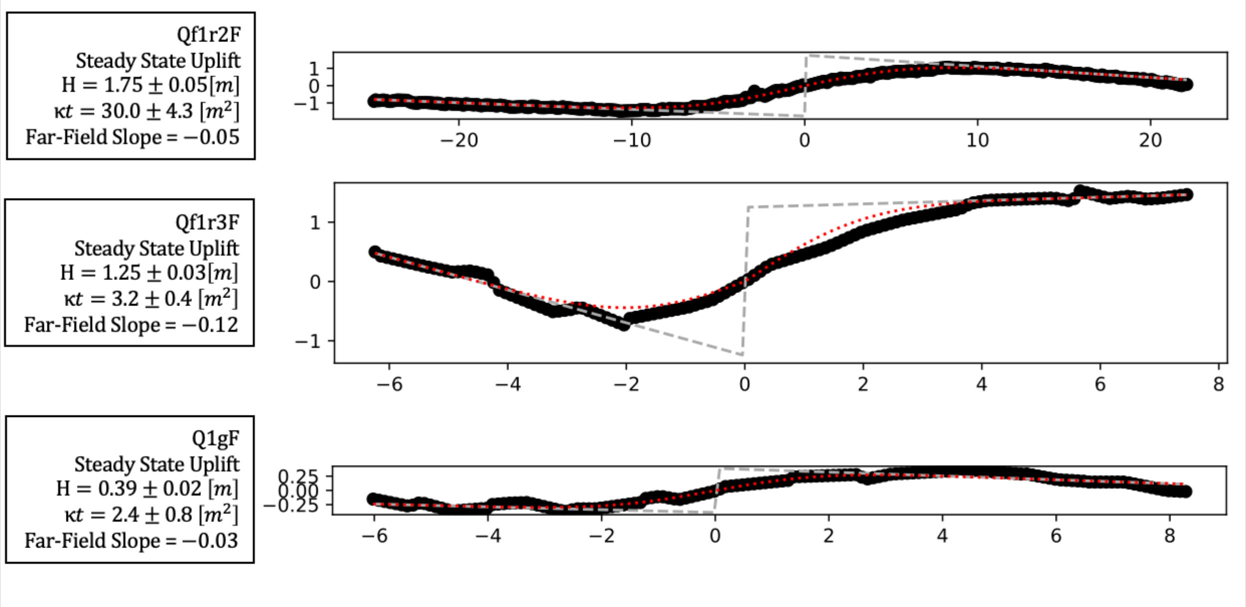

Figure 4-14. Extracted scarp profile from map location F, analyzed under steady state uplift conditions: (1) Qf1r2F, (2) Qf1r3F, (3) Q1gF.

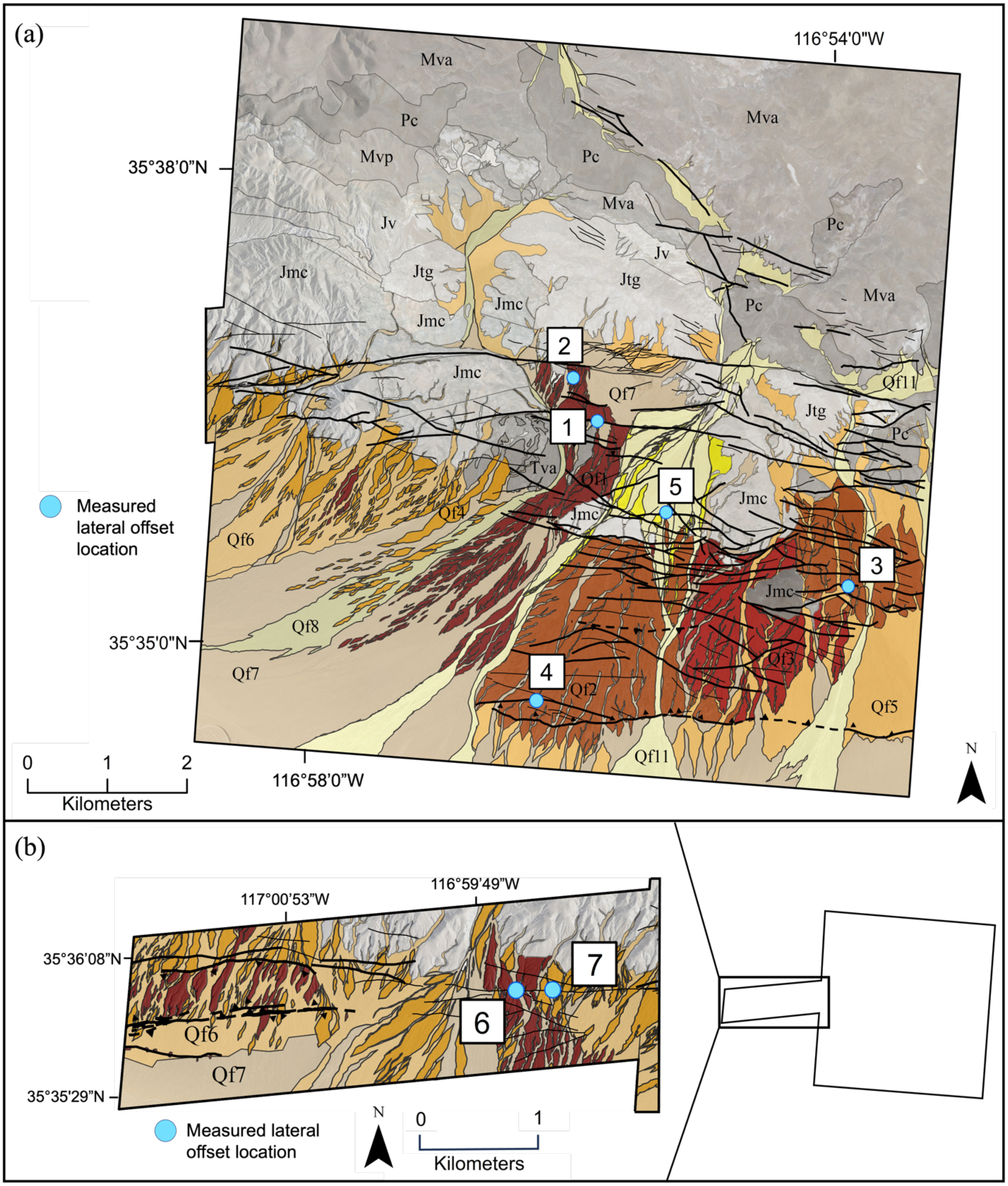

Figure 4-15. Geologic map with measured lateral offset locations indicated (Locations #1-7). See Figure 4-16 for LiDAR hillshade maps of each location's measured offset.

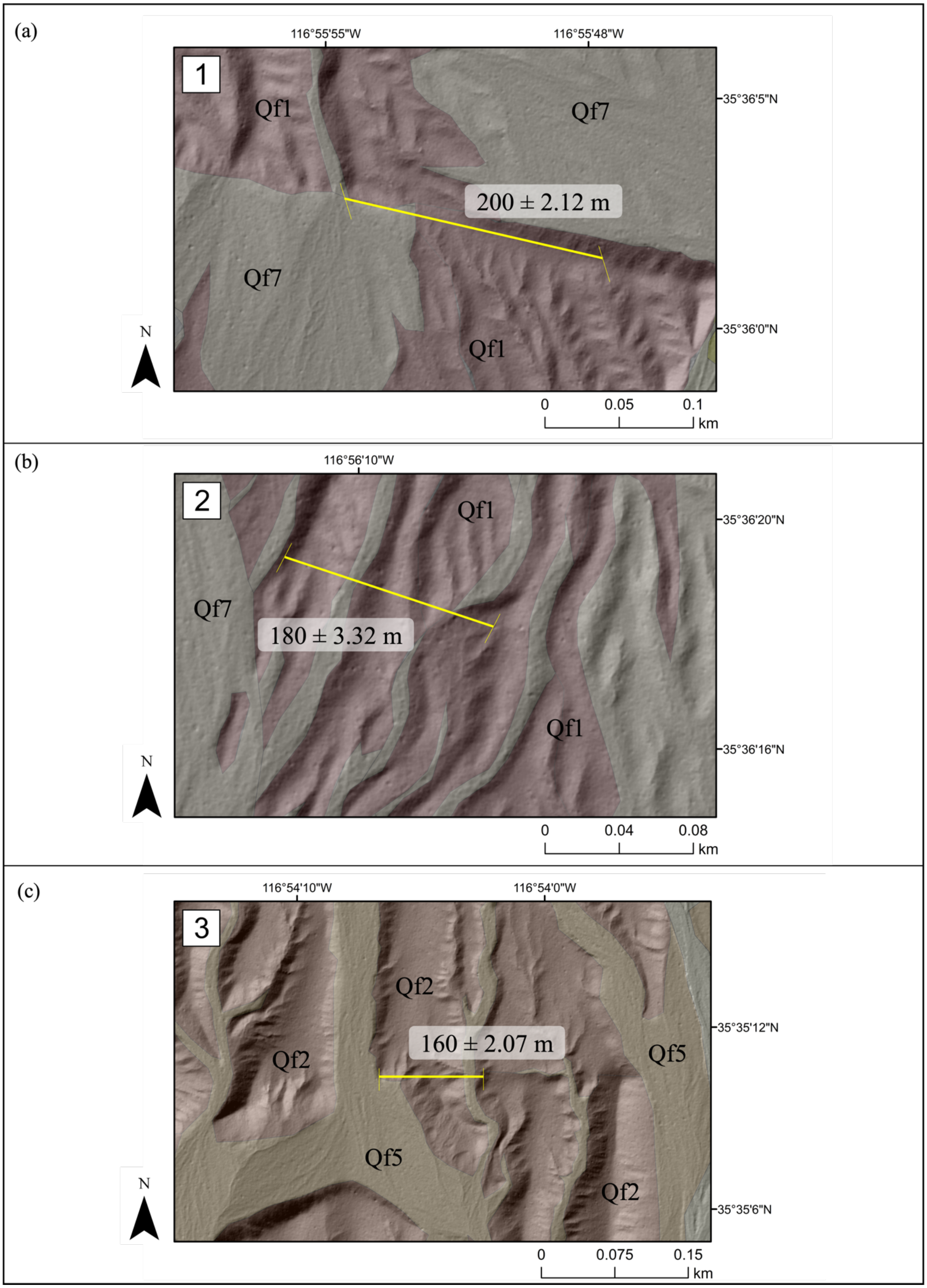
(a)
1
116°55'55"W
116°55'48"W
35°36'5"N
35°36'0"N
Qf1
Qf7
200 ± 2.12 m
Qf7
Qf1
N
0
0.05
0.1
km
(b)
2
116°56'10"W
35°36'20"N
35°36'16"N
Qf1
Qf7
180 ± 3.32 m
Qf1
N
0
0.04
0.08
km
(c)
3
116°54'10"W
116°54'0"W
35°35'12"N
35°35'6"N
Qf2
Qf2
160 ± 2.07 m
Qf5
Qf5
Qf2
N
0
0.075
0.15
km

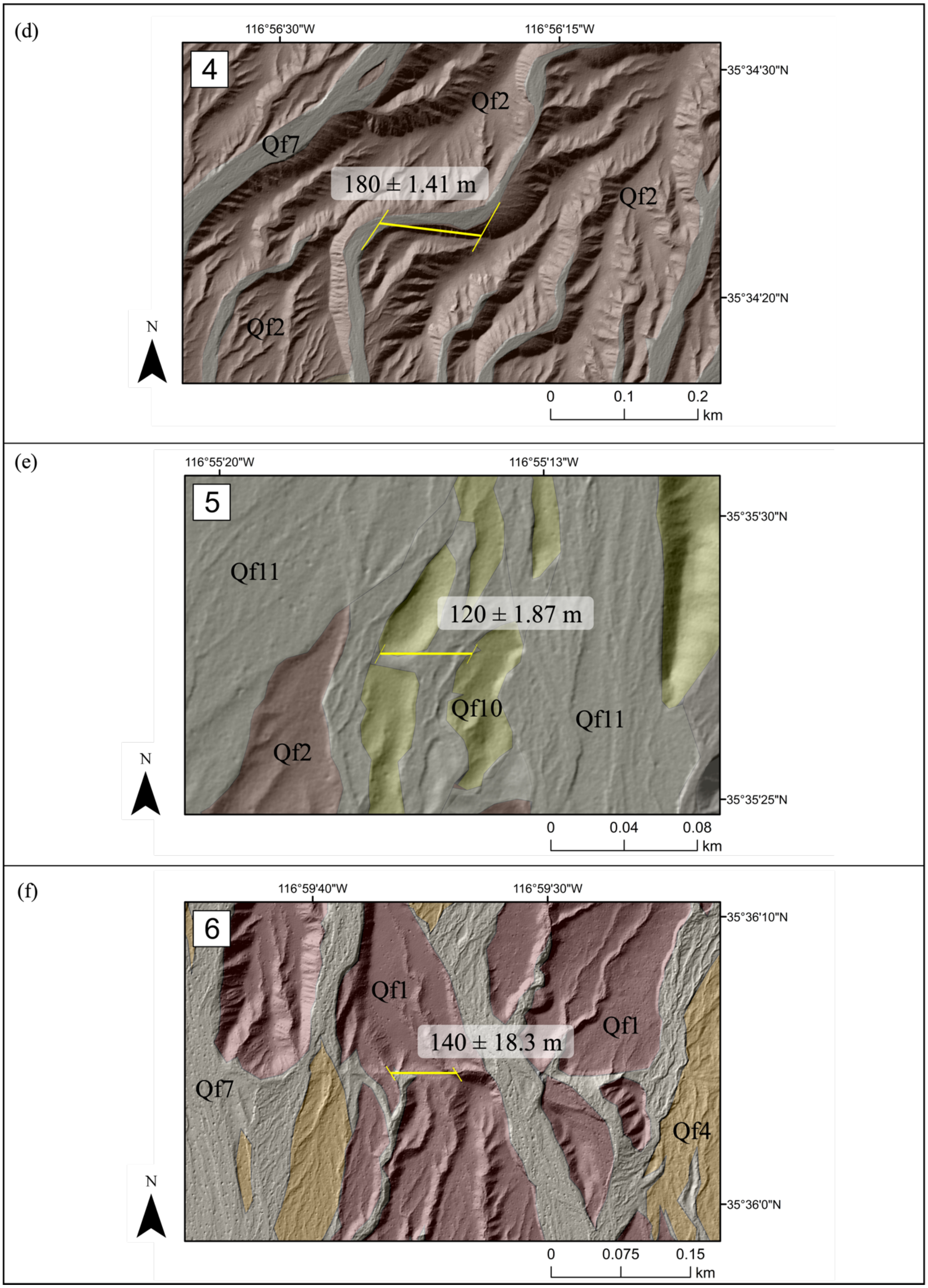
(d)
116°56'30"W
116°56'15"W
35°34'30"N
35°34'20"N
4
Qf2
Qf7
180 ± 1.41 m
Qf2
Qf2
N
0
0.1
0.2
km
(e)
116°55'20"W
116°55'13"W
35°35'30"N
35°35'25"N
5
Qf11
120 ± 1.87 m
Qf10
Qf11
Qf2
N
0
0.04
0.08
km
(f)
116°59'40"W
116°59'30"W
35°36'10"N
35°36'0"N
6
Qf1
Qf1
140 ± 18.3 m
Qf7
Qf4
N
0
0.075
0.15
km

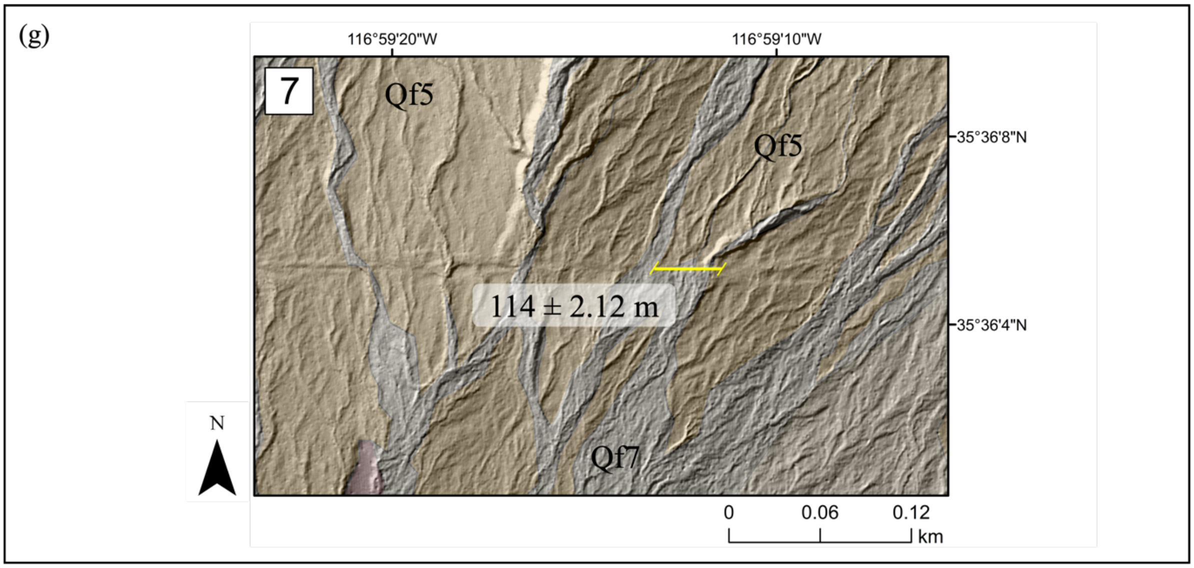

Figure 4-16. LiDAR hillshade maps of each measured lateral offset, measured offset is highlighted in yellow and labeled with the average measurement: (a) Location 1; (b) Location 2; (c) Location 3; (d) Location 4; (e) Location 5; (f) Location 6; (g) Location 7. See Table 4-2 for individual offset measurements.

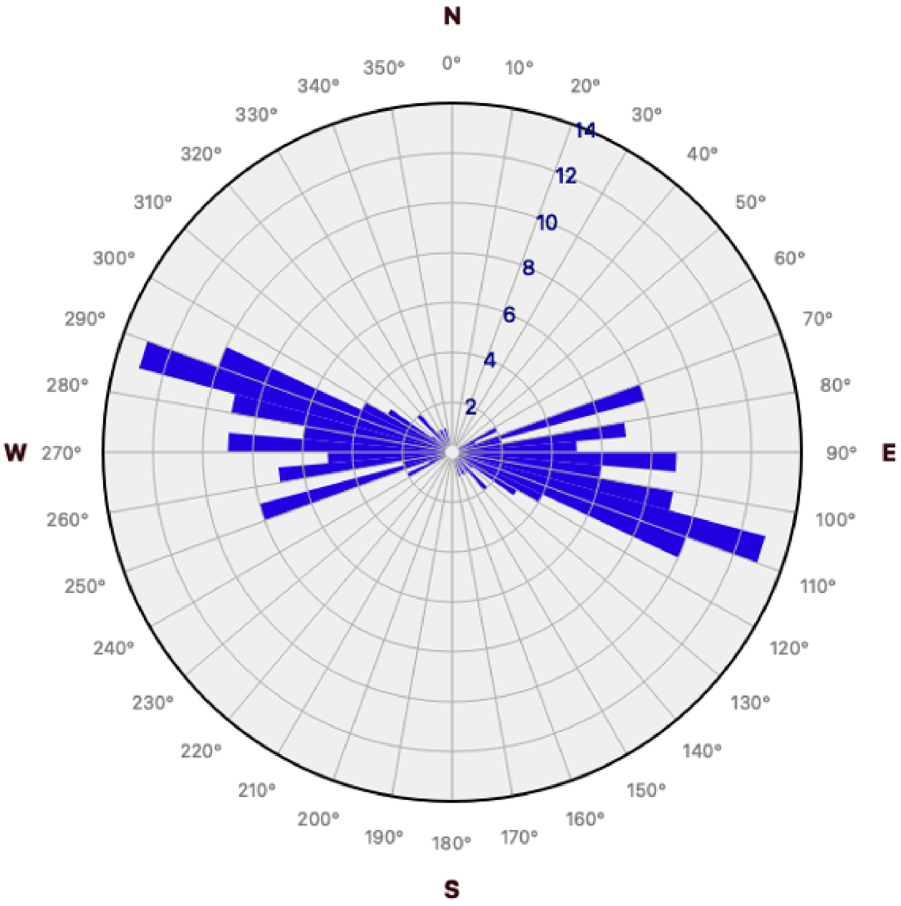

Figure 4-17. Rose diagram of the orientations of the strike-slip faults in the mapping region. Accounted for in this figure are the 85 identified strike slip faults, both right-lateral and left-lateral sense. The dominant trend of these structures is east-west trending, with an average strike of 099.

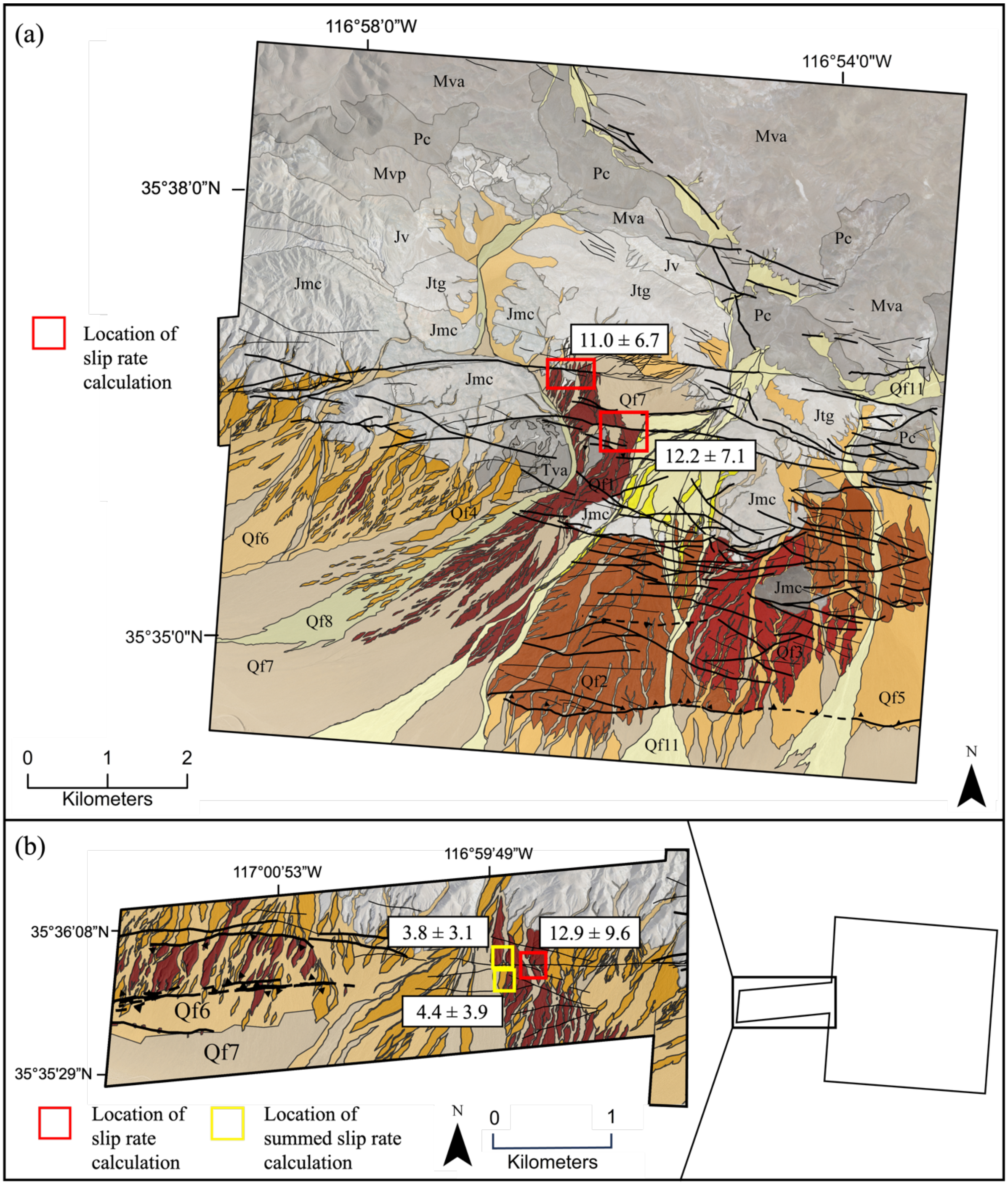

Figure 4-18. Geologic map of the intersection of the Brown Mountain fault and the Garlock fault with the locations of slip-rate measurements highlighted. Red boxes indicated the measurement was taken as a single strand slip rate, yellow boxes indicate the slip rates were summed together as multiple branches of the larger fault strand.

Table 4-1. Mapped Alluvial Unit Characteristics

Alluvial Unit	Apparent Relief	Surface Roughness Values		
		Min.	Max.	Mean
1	high	0	0.65	0.46
2	high	0.53	1.35	0.82
3	high	0.57	1.94	0.88
4	moderate	1.2	3.45	2.17
5	low	1.14	4.05	2.74
6	low	1.28	4.85	3.41
7	low	1.47	5.77	4.08
8	low	3.46	7.84	4.69
9	none	3.26	6.48	5.13
10	none	2.74	9.79	6.90

Table 4-2. Left Lateral Offset Measurements

Map Location Label	Offset Alluvial Unit	Offset Measurements (meters)			
		Individual Measurements[1]	Minimum	Maximum	Average
1	Qf1	198 198 200 201 203	198	203	200.5
2	Qf1	175 179 181 181 184	175	184	179.5
3	Qf2	157 160 161 162 162	157	162	159.5
4	Qf2	178 180 180 180 182	178	182	180
5	Qf10	117 118 119 119 122	117	122	119.5
6	Qf1	116 126 143 144 164	116	164	140
7	Qf4	111 111 113 114 116	111	116	113.5

[1] In order to account for errors (see text for error descriptions), five measurements were taken in each location and reported as an minimum, maxiumum, and average.

Table 4-3. Scarp degradation analysis results, left-lateral fault scarps

Map Location Label	Profile ID	Upper Alluvial Unit	Lower Alluvial Unit	Offset Height, H (m)	Total Degradation, κt (m^2)	Uplift Analysis
A	Qf1r1A	Qf1	Qf7	2.29 ± 0.04	5.1 ± 0.4	single event
A	Qf7rb2A	Qf7	Qf7	0.22	0.6	single event
A	Qf7rb3A	Qf7	Qf7	0.55	1.5	single event
B	Qf25r2B	Qf2	Qf5	3.2	21.7	single event
D	Qf1r4D	Qf1	Qf1	2.01 ± 0.06	25.5 ± 4.2	steady state
D		Qf1	Qf1		11.3 ± 1.7	single event
D	Qf14r2D	Qf1	Qf4	0.88 ± 0.03	2.4 ± 0.5	single event
D	Qf17r1D	Qf1	Qf7	3.93 ± 0.04	12.2 ± 0.6	single event
D	Qf17r2D	Qf1	Qf7	1.65 ± 0.05	3.9 ± 0.6	single event
D	Qf17r3D	Qf1	Qf7	1.46 ± 0.03	1.00	single event

Table 4-4. Calculated ages of left-lateral scarp profiles

Map Location Label	Profile ID	Upper Alluvial Unit	Lower Alluvial Unit	Total Degradation, κt (m^2)	Calculated Age (kyr)	Uplift Analysis
A	Qf1r1A	Qf1	Qf7	5.1 ± 0.4	19.6 ± 7.8	single event
A	Qf7rb2A	Qf7	Qf7	0.6	2.23 ± 0.8	single event
A	Qf7rb3A	Qf7	Qf7	1.5	5.6 ± 1.9	single event
B	Qf25r2B	Qf2	Qf5	21.7	81.4 ± 27.1	single event
D	Qf1r4D	Qf1	Qf1	11.3 ± 1.7	44.5 ± 20.5	single event
				25.5 ± 4.2	101 ± 47.6	steady state
D	Qf14r2D	Qf1	Qf4	2.4 ± 0.5	9.6 ± 4.9	single event
D	Qf17r1D	Qf1	Qf7	12.2 ± 0.6	46.5 ± 17.5	single event
D	Qf17r2D	Qf1	Qf7	3.9 ± 0.6	15.4 ± 7.1	single event
D	Qf17r3D	Qf1	Qf7	1.00	3.8 ± 1.3	single event

Table 4-5. Scarp degradation analysis results, dip-slip fault scarps

Map Location Label	Profile ID	Upper Alluvial Unit	Lower Alluvial Unit	Offset Height, H (m)	Total Degradation, κt (m^2)	Uplift Analysis
E	Qf3t1E	Qf2	Qf2	1.59 ± 0.03	20.4 ± 1.2	single event
E	Qf3t1E	Qf2	Qf2	1.59 ± 0.03	46.5 ± 3.3	steady state
F	Qf1r2F	Qf1	Qf1	1.75 ± 0.05	30 ± 4.3	steady state
F	Qf1r2F	Qf1	Qf1	1.75 ± 0.05	13.1 ± 1.5	single event
F	Qf1r3F	Qf1	Qf1	1.25 ± 0.03	3.2 ± 0.4	steady state
F	Qf1r3F	Qf1	Qf1	1.25 ± 0.05	1.2 ± 0.4	single event
F	Qf1gF	Qf1	Qf1	0.39 ± 0.02	2.4 ± 0.8	steady state
F	Qf1gF	Qf1	Qf1	0.39 ± 0.02	1.1 ± 0.3	single event

Table 4-6. Calculated ages of dip-slip scarp profiles

Map Location Label	Profile ID	Upper Alluvial Unit	Lower Alluvial Unit	Total Degradation, κt (m^2)	Calculated Age (kyr)	Uplift Analysis
E	Qf3t1E	Qf2	Qf2	20.4 ± 1.2	78 ± 30	single event
				46.5 ± 3.3	179 ± 71	steady state
F	Qf1r2F	Qf1	Qf1	13.1 ± 1.5	51 ± 22	single event
				30 ± 4.3	118 ± 54	steady state
F	Qf1r3F	Qf1	Qf1	1.2 ± 0.4	5.0 ± 3.0	single event
				3.2 ± 0.4	12.5 ± 5.5	steady state
F	Qf1gF	Qf1	Qf1	1.1 ± 0.3	4.5 ± 2.5	single event
				2.4 ± 0.8	10.0 ± 6.0	steady state

Table 4-7. Vertical Slip Rate Measurements

Map Location Label	Reverse Fault Profile ID	Offset Height, H (m)	Scarp Age (kyr)	Vertical Slip Rate (mm/yr)
E	Qf3t1E	1.59 ± 0.03	78 ± 42.4	0.024 ± 0.014
F	Qf1r2F	1.75 ± 0.05	51 ± 31.1	0.043 ± 0.028
F	Qf1r3F	1.25 ± 0.03	5.0 ± 4.2	0.39 ± 0.34
F	Qf1gF	0.39 ± 0.02	4.5 ± 3.5	0.13 ± 0.10
			Average Vertical Slip Rate:	0.15 ± 0.12 mm/yr

Table 4-8. Calculated slip rate along the Garlock Fault

Lateral Offset Location	Offset Measurement (m)	Correlated Scarp Profile	Uplift Analysis	Scarp Age (ka)	Calculated Slip Rate (mm/yr)	Summed Slip Rate (mm/yr)
6	140 ± 33.94	Qf1r4D	single event	44.5 ± 20.5	4.4 ± 3.9[†]	8.2 ± 3.5
6	140 ± 33.94	Qf17r1D		46.5 ± 17.5	3.8 ± 3.1[†]	
6	140 ± 33.94	Qf17r2D	single event	15.4 ± 7.1	12.9 ± 9.6	
1	200.5 ± 3.53	Qf1r1A	single event	19.63 ± 7.8	12.2 ± 7.1	
2	179.5 ± 6.36	Qf1r1A	single event	19.63 ± 7.8	11.0 ± 6.7	
		Average Slip Rate along the Garlock Fault:			11.1 ± 6.7 mm/yr	

[†] Indicates multi-stranded segments of the Garlock fault that are summed together to yield overall Garlock slip rate

5. DISCUSSION

5.1. Geologic Map Analysis

5.1.1. Mapped Alluvial Units

In the created geologic map, ten alluvial units in the region were delineated. Movement along these units, and bracketed minimum ages, range from 3.8 ± 1.3 kyr to 178 ± 70.5 kyr. Of the alluvial units that contained extracted profiles, which included Qf1, Qf2, and Qf7, the calculated minimum ages corresponded to the assigned relationships of relative ages. The largest magnitude calculated from the scarp degradation actually correlated to the unit Qf2 (178 ± 70.5 kyr) however, the magnitude of the largest value for Qf1 was very similar to Qf2 (172 ± 58 kyr). Given the large margin of error of the calculation from Qf2, and the additional largest calculated ages for both Qf1 (~53 -170 kyr) and Qf2 (~48 – 110 kyr), Qf1 can be deemed older than Qf2 with some confidence. Alluvial unit Qf7 yielded a maximum age of 5.7 ± 1.8 kyr, making it the youngest analyzed unit. It is important to note that in order to form a more complete picture of age relationships, more scarp profiles should be extracted to bracket ages on the additional alluvial units. Another important note is that these units were differentiated based on surface ages, and not geologic composition. It is possible, as seen in other published maps of the region (e.g. Andrew, 2007), that the identified units have the same geologic composition, or are from the same geologic provenance, but have different surface ages.

5.1.2. Fault Geometry

The mapped faults within the region give insight into how the regional structures and stress regimes interact with one another. Both the strike-slip and dip-slip fault structures are integral pieces of information to understand the overall sense of stress in the region, in both direction and magnitude, and how strain is partitioned from the collision of the Pacific and North American tectonic plates.

5.1.3 Contractional Structures

Within the mapping region the identified dip-slip structures are reverse faults. The identified reverse faults all strike east-west, having an average strike of 083, and no observed dip slip faults striking in the north-south or northwest-southeast direction. With reverse faults in this orientation, the required orientation of the maximum principal stress would be in the north-south direction. Compressional stresses in the north-south direction aligns with regional movement from the Eastern California shear zone. The east-west strike of these traces suggests they are possible reactivated fault structures that were originally lateral strike-slip faults that became reverse faults as the north-south compression caused failure in the region. The average slip rate along these dip-slip structures is 0.15 ± 0.12 mm/yr, with a minimum slip rate of 0.024 ± 0.014 mm/yr on profile Qf3t1E, which encompasses the large fold scarp in the southern portion of the mapping region, and a maximum slip rate of 0.39 ± 0.34 mm/yr on profile Qf1r3F in the western section of the map. This implies that movement on these structures is geologically slow compared to the surrounding regional fault structures. The compressional stresses acting in-line with the Eastern California shear zone are active in this region, and the calculated slip value is comparable to other measurements of vertical motion within the Eastern California shear zone (0.1-0.6 mm/yr).

5.1.4. Fault Truncations

The identified strike-slip faults in the central map region are both east-west striking Garlock fault-associated traces and northwest-southeast striking Brown Mountain fault-Eastern California shear zone-associated faults. Although not universally seen throughout the map region, the dominant trend is that the northwest-southeast fault traces truncate at the east-west striking fault traces. The average slip rate along the left-lateral, Garlock-associated scarp profiles is 7.77 ± 5.2 mm/yr. The minimum calculated rate is 2.2 ± 1.1 mm/y extracted from profile Qf25r2B across the offset alluvial unit Qf2 in the eastern portion of the map at location B. The maximum calculated slip rate is 12.9 ± 9.6 mm/yr extracted from profile Qf17r2D across alluvial unit Qf1 located in the western portion of the mapping region at location F.

From the analysis of the reverse fault scarp profiles, it is evident that both the strike-slip and dip-slip structures have been active in the same relative time frame. However, the slip rates of these different structures, combined with the dominant trend of Garlock-associated fault traces truncating the Eastern California shear zone-associated traces suggests that stress is largely partitioned along the east-west trending structures. Strain is accumulating and releasing within both regions in the Holocene time; however, the more recent and dominant activity can be found along the east-west striking segments of the Garlock fault.

5.2. Geologic Slip Rate of the Garlock Fault

5.2.1. Calculated Slip Rates

Of the six individual measurements of left-lateral slip along the Garlock fault, the results can be partitioned into two groups: (1) fast slip rates of 11.0 ± 6.7 mm/yr, 12.2 ± 7.1 mm/yr, and 12.9 ± 9.6 mm/y; and (2) slow slip rates of 2.2 ± 1.1 mm/yr, 3.8 ± 3.1 mm/yr, and 4.4 ± 3.9 mm/yr. The laterally offset alluvial unit in all of these measurements is either Qf1 or Qf2, the oldest designated map units. There appears to be no correlation between the fast and slow slip rate groupings and ages of alluvial fans. It is likely the profiles that yielded the slower slip rates are across fault traces that have not recently activated, as all the profiles used for the three slow calculations have much older ages ranging between ~40-80 kyr as opposed to the faster measurements' ages (~15-20 kyr). In more recent Holocene time, it is most likely the higher magnitude slip rate values are more valid. The average of the calculated slip rates that are of larger magnitude is 12.0 ± 7.8 mm/yr. From the Late Pleistocene to Holocene time, all calculated values can be included in calculating the average magnitude of slip along the Garlock fault.

5.2.2. Slip Magnitudes along the Garlock Fault

The average calculated slip rate from this study along the east-west segments of the Garlock fault within the Late Pliestocene-Holocene time is 11 ± 6.7 mm/yr. In order to capture the complete picture of the slip rate along the entirety of the Garlock fault, this calculated value should be compared with rates from other study sites along the Garlock fault (Figure 5-1, Table 5-1). Of the reported studies encompassing the western Garlock fault (Clark and Lajoie (1974); McGill et al. (2009)) the average reported slip rate is 7.45 ± 2.9 mm/yr. Along the central sections of the Garlock fault, the average reported slip rate is 7.92 ± 4.1 mm/yr, with rates as high as 14 mm/yr (McGill and Sieh (1993); Ganev et al. (2012); Rittasse et al. (2014)). The calculated value from this study is comparable to the average rates reported in the western and central sections of the Garlock fault. This suggests that the slip rate along the entirety of the Garlock fault is relatively constant from the west to the eastern segments.

Although values of geologic slip rate are comparable across the fault system, geodetic measurements suggest movement along the fault is substantially slower than these reported values, approximately ~1-3 mm/yr. This discrepancy has two possible explanations: (1) the strain accumulation discrepancy means the Garlock fault system is late in its earthquake cycle, and (2) accumulation of strain within the Eastern California shear zone has only recently become active. One or both of these explanations may be valid. If the Garlock is late in its earthquake cycle, this has implications for the seismic hazards within the region, indicating a large magnitude rupture may be imminent. If the second explanation is valid, it would lead to implications for how the North American-Pacific plate boundary interaction has been partitioning strain in the region.

5.2.1. Regional Kinematic Implications

In order to understand the broader kinematics of southern and eastern California, the slip rate along the Garlock fault can be compared to the larger fault networks of the Eastern California shear zone (Table 5-2). From highest to lowest slip rate: (1) the Garlock fault, (2) Central Death Valley-Furnace Creek Fault Zone, (3) Owens Valley fault zone, (4) the Owl Lake fault, (5) the Brown Mountain fault, (6) Panamint Valley fault zone (Figure 5-2). There is no obvious trend of directionality in an increase or decrease of slip rate along the trace of the Garlock fault. Additionally, the fault systems associated with the northern Eastern California shear zone all have slower slip rates than the Garlock fault, with the slowest reported rate being the centermost fault regional system (Panamint Valley fault zone). This further suggests strain is being partitioned more into the east-west Garlock fault structures in the region.

Returning to the hypotheses presented in Figure 1-2, the calculated slip rate along the central Garlock fault will help determine which model best fits the overall kinematics of the Garlock fault. The first hypothesis, the ‘conjugate fault’ model, states that the dextral fault systems north of the Garlock fault (i.e. Owens Valley, Panamint Valley, Death Valley) will have similar slip rates to the Garlock fault at the point at which they intersect with the Garlock fault trace. These northern fault systems have significantly smaller slip rates than the Garlock fault at all points along its trace, making this hypothesis unlikely. The second hypothesis, the ‘transform fault’ model, requires a decreasing slip rate from the western segments of the Garlock fault to the eastern segments, corresponding to extension within the Basin and Range province. The calculated slip rate from this study suggests the Garlock fault has a nearly constant slip rate along its trace, making the second hypothesis unlikely to fit the regional kinematics. The third hypothesis, the 'clockwise rotation' model, requires a constant slip along the entirety of the Garlock fault in order to account for a constant clockwise rotation of the southern Mojave block. The results of this study show the previously published slip rates of the eastern Garlock fault are of similar magnitude to those in the eastern segments. Therefore, of the three proposed hypothesis, the results of this study agree most closely with the 'clockwise rotation' model, where strain is being partitioned along the Garlock fault not only from the Pacific-North American plate boundary collision, but most significantly from the Mojave Block clockwise rotation, causing a near-constant slip along the entire trace of the Garlock fault. The higher reported slip rate in Holocene time also alludes to shifts in regional kinematic behavior more recently. It is worth noting, the large error margin within the reported slip rate makes it such that any certainty in kinematic relationships cannot be defined with significant confidence.

5.2. Limitations of Study

The efforts to complete a geologic map from entirely remotely-sensed data sources does not come without some substantial assumptions that can propagate error into the results of the study. There are three main sources of error that are worth discussing in this study: (1) remote sensing limitations; (2) extrapolation of mapping to the numerical data set; (3) diffusion analysis assumptions.

In a study designed with intention to test the viability of remotely-sensed data for geologic mapping and establishing age relationships, it is necessary to address the error that exists within the produced map product. The biggest potential source is the availability and extent of the remotely-sensed data sources. LiDAR data, unlike NAIP data sets, has not been universally applied to the geographic extent of the United States. The availability of LiDAR data is entirely dependent on previously conducted studies within the desired region, or having the financial ability and resources to conduct a site-specific study. In this study, the LiDAR point cloud was taken from a previously conducted LiDAR swath over the Garlock fault and surrounding region. While the LiDAR study encompasses the majority of the mapping area, approximately 25% of the mapping region is not covered by the study. This missing data is primarily in the northern section that has already been mapped as bedrock, which was not the focus of this study. However, there are alluvial units within this area that were not able to be analyzed by the hillshade, slope map, and surface roughness analysis because of this LiDAR limitation. An additional component to geologic mapping is including detailed unit descriptions of composition and characteristics of the mapped units. In the case of the utilized remotely-sensed data sets, universally and for this study too, the ability to handle and analyze the different alluvial products was not possible. Physically inspecting the different rock morphologies would be an additional way to create a robust data set and corroborate different choices for age characteristics. In this study, the unit descriptions were taken from generalized geologic maps of the region, and these unit descriptions are a limitation in the completeness of the analysis.

The next primary source of error is extrapolating numerical measurements from the created mapping product. Taking quantitative measurements of lateral offset from the map product depends on accuracy in both the mapped alluvial unit extents and measuring tool within the software. Error within both of these measures will propagate into the calculated slip rates along the strike-slip faults. Additionally, an added source of error comes from the extrapolation between the lateral offsets and correlated scarp profiles when calculating the lateral slip rates. For the entirety of the slip rate calculations, scarp profiles were chosen to be as geographically close to the measured lateral offsets as possible. However, for some profiles, specifically in location F, data from the nearest lateral offset was approximately 2 km away from the profiles.

The final, major source of error was in the scarp degradation analysis. It is important to note that this method of calculating timing of movement along the scarp profiles only yields the minimum age on each. This means that the calculated scarp ages are minimum estimates, which propagates into the slip-rate calculations and yields the maximum estimated slip rates in the region. In the same vein, the choice of steady state analysis versus steady state analysis for modeling will influence the estimated age of the profile. The steady-state uplift model approximates slow creep along fault traces, whereas the single event model approximates a single rupture event. The steady state model yields much older ages than the single event model, which would yield slip rates that are too slow. Neither of these end members can accurately approximate the behavior of the faults in the mapping region, however due to the low seismicity in the region, and the observation that the fault networks rupture in clusters, the ages used for slip-rate estimates are from the single-event model.

Finally, a non-trivial assumption that was made for this study was the value of the diffusivity constant, $\boldsymbol{\kappa}$, for the scarp diffusion analysis. For the calculations presented, the constant value was approximated based on geographic and climatic proximity of the study area from Frankel et al. (2015), and the region of focus in this study. The primary concerns for choosing a $\boldsymbol{\kappa}$ value hinged on the general topological processes occurring and the amount of rainfall within the region. Errors in choosing the $\boldsymbol{\kappa}$ value will cause the scarp profile ages, and therefore the calculated slip rates, to be erroneous. In the calculation of the profile ages, a $\boldsymbol{\kappa}$ value that is too high will cause the ages to be too young, and if the $\boldsymbol{\kappa}$ value is too low, the calculated ages will be too old. Conversely, these errors propagate into the slip rate calculations in an inverse manner. If the approximated $\boldsymbol{\kappa}$ is too high, slip rates will report too fast; if $\boldsymbol{\kappa}$ is too low, slip rates will be too slow. In order to have more certainty in the calculated timings of movement along the faults in the region, focused studies in the region should better constrain $\boldsymbol{\kappa}$.

5.3. Future Work

A final goal of the study is to calibrate and assess the accuracy of remotely collected data, specifically surface roughness, to determine the absolute ages of alluvial fan surfaces in arid environments. Acquiring absolute ages of samples requires both field and laboratory resources and investment; from choosing a viable and safe field site, to collecting valid test samples and then crushing, milling and analyzing such samples. These efforts are incredibly time-consuming and require a significant amount of budget resources. Therefore, it is the intention that this study's findings will aid in the development of a surface roughness-age model for rock surfaces in arid environments.

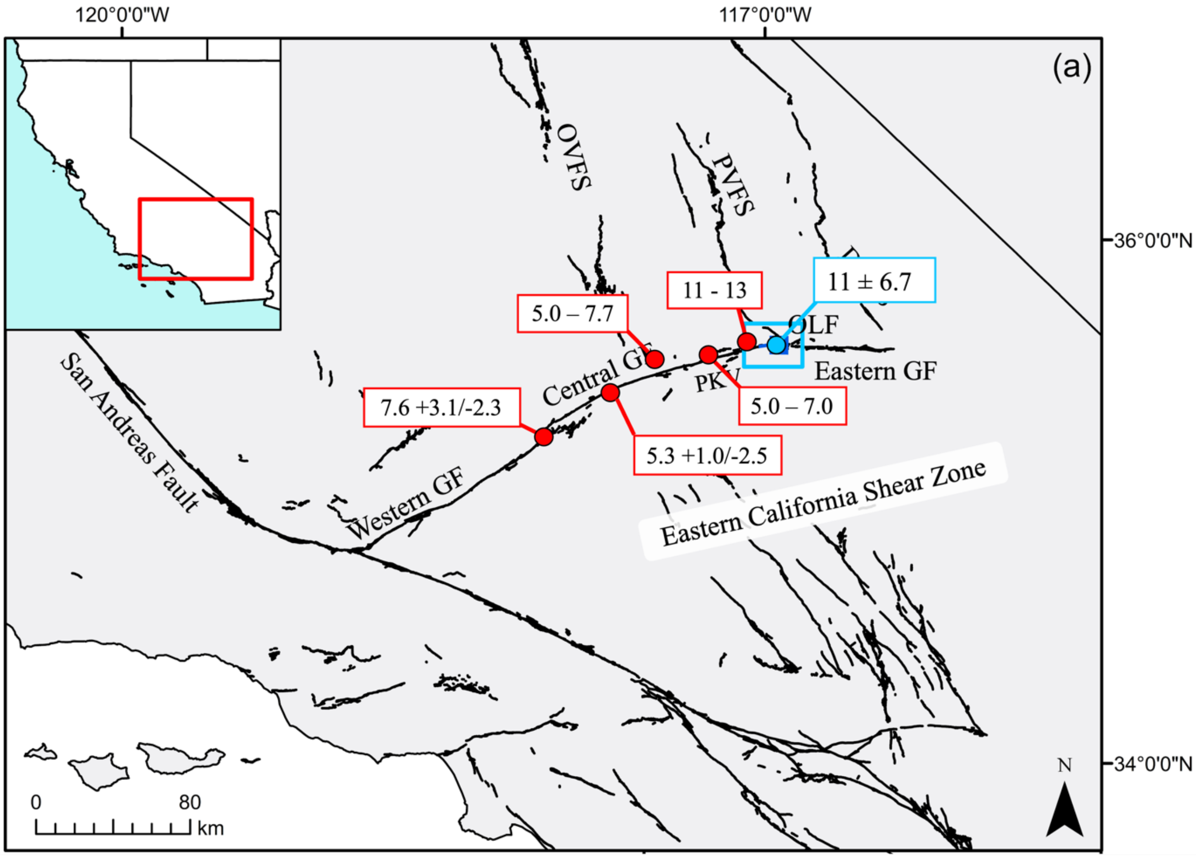

Figure 5-1. Map of previously reported slip rates along the Garlock Fault, shown in red, and the calculated slip rate from this study, shown in blue. See Table 5-1 for information about each slip rate and the associated study.

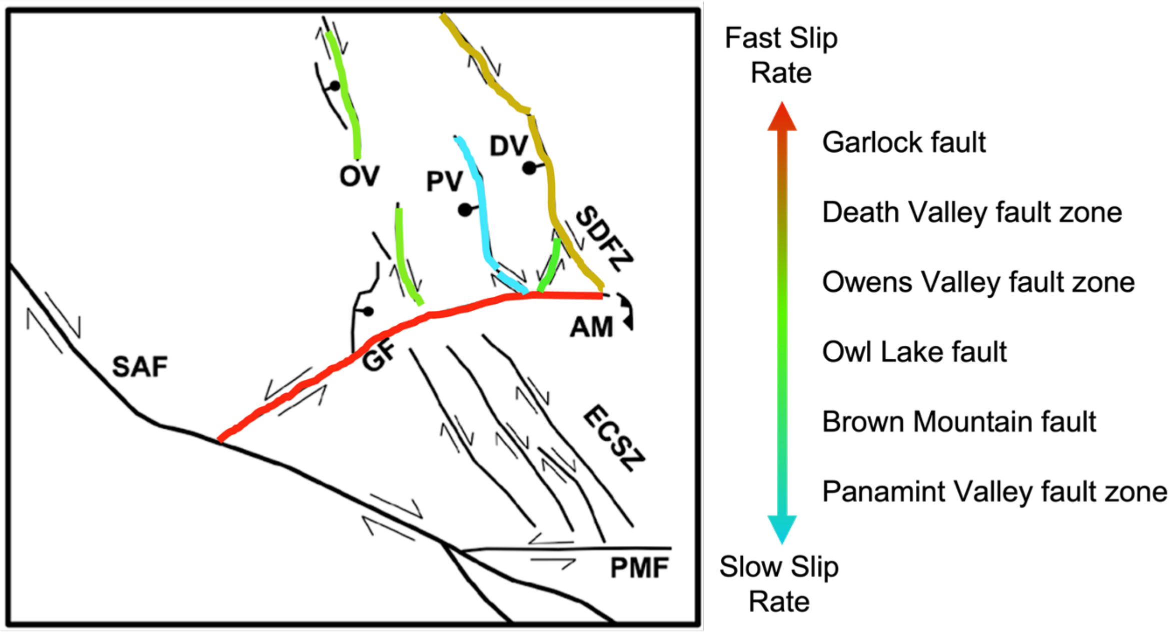

Figure 5-2. Comparison of regional fault zone slip rates. The fastest slip rate is shown in red (the Garlock fault) and the slowest slip rate is shown in blue (Panamint Valley fault zone), with the intermediate value shown as green.

Table 5-1. Previously reported slip rates along the Garlock fault

Study	Study Location	Garlock Fault Segment	Reported Slip Rate (mm/yr)
McGill et al. (2009)	Clark Wash	West	7.6 +3.1/-2.3
Clark and Lajoie (1974)	Koehn Lake	West	5.0 - 7.7
Ganev et al. (2012)	Summit Range	Central	5.3 +1.0/-2.5
McGill and Sieh (1993)	Searles Lake	Central	4.0 - 9.0
Rittasse et al. (2014)	Pilot Knob Valley	Central	11 - 13
Murphy (2023)	Eastern Quail Mnt.		11.1 ± 6.7

Table 5-2. Slip rate values for larger fault structures in southern and eastern California[1]

Fault System	Slip Sense	Slip Rate (mm/yr)
Garlock Fault		
Eastern segment[2]	Left-lateral	7.77 ± 5.2
Central segment		7.92 ± 4.1
Western segment		7.45 ± 2.9
The Death Valley-Furnace Creek Fault Zone		
Central segment	Right-lateral	4.85 ± 1.06
Northern terminus (Fish Lake Valley)		2.75 ± 0.35
Owl Lake Fault	Left-lateral	2.0 ± 1.41
Panamint Valley Fault Zone		
Central segment	Right-lateral	1.74 ± 0.65
Southern terminous (Brown Mountain fault)		1.88 ± 0.18
Owens Valley Fault Zone	Right-lateral	2.5 ± 2.12

[1] Values are from the Geologic Background section of this report

[2] Reported value is the calculated slip rate fromm this study

6. CONCLUSIONS

In this study, a geologic map of the intersection between the east-west striking Garlock fault and northwest-southeast striking Brown Mountain fault is presented to better understand the regional kinematics of the larger Garlock fault system. Within the mapping extent, 139 total faults were identified consisting of both strike slip and dip slip faults. From the created geologic map, seven locations of lateral offset were identified and measured and seventeen scarp profiles were extracted from the mapping extent to constrain the timing of the latest movement along the fault scarps and terrace risers.

Using both offset measurements and timing calculations, the slip rate along the east-west striking Garlock fault was calculated to be 7.77 ± 5.2 mm/yr. This value is comparable to the previously reported values of the western and central Garlock fault segments. Of the strike-slip faults, the dominant trend in the mapping area showed the east-west striking Garlock-associated faults truncating the northwest-southeast Eastern California shear zone-associated faults. Given the geometry and timing of the different structures in the region, it is likely that both the Eastern California shear zone and the Garlock fault are active in the current time frame, however the most recent activity and larger magnitude of strain partitioning occurs along the east-west striking Garlock fault. Reported geologic slip rates along the Garlock fault are much slower than the calculated and previously reported slip rates. The implications for this assessment are that the Garlock fault is in the late stages of its earthquake cycle, and that a large magnitude rupture could be imminent and/or that strain partitioning onto the structures within the Eastern California shear zone is a relatively new process.

Of the proposed kinematic models, the data in this study suggests the Garlock fault kinematics best fit the ‘clockwise rotation’ regional model. In this model, due to the southern

Mojave block’s constant clockwise rotation, a constant left-lateral slip rate is induced over the entire trace of the Garlock fault. The established near-constant slip rate of the Garlock fault and concurrent activity with the Mojave block indicate the major constituent contributing to strain partitioning along the Garlock fault is the clockwise rotation of the Mojave Desert Block.

REFERENCES

Andrew, J.E. “Western Quail Mountains Geological Map.” 1:12,000. Geological Society of America, 2007.

Andrew, JE, WM Rittase, FM Monastero, T Bidgoli, and JD Walker. “Geologic Map of the Northern Lava Mountains and Summit Range, San Bernardino County, California: Geological Society of America Digital Map and Chart 19, Scale 1: 20,000, Doi: 10. 1130/2014.” *DMCH019*, 2014.

Andrew, JE, WM Rittase, and JD Walker. “Geologic Map of the Southern Slate Range and a Portion of the Central Garlock Fault, China Lake Naval Weapons Station, San Bernardino County, California,” 2014.

Andrew, Joseph E., and J. Douglas Walker. “Reconstructing Late Cenozoic Deformation in Central Panamint Valley, California: Evolution of Slip Partitioning in the Walker Lane.” *Geosphere* 5, no. 3 (June 1, 2009): 172–98. https://doi.org/10.1130/GES00178.1.

Andrews, D. J., and T. C. Hanks. “Scarp Degraded by Linear Diffusion: Inverse Solution for Age.” *Journal of Geophysical Research: Solid Earth* 90, no. B12 (October 10, 1985): 10193–208. https://doi.org/10.1029/JB090iB12p10193.

Bacon, Steven N., and Silvio K. Pezzopane. “A 25,000-Year Record of Earthquakes on the OwensValley Fault near Lone Pine, California: Implications for Recurrence Intervals, Slip Rates, and Segmentation Models.” *GSA Bulletin* 119, no. 7–8 (July 1, 2007): 823–47. https://doi.org/10.1130 /B25879.1.

Barnhart, William D., Gavin P. Hayes, and Ryan D. Gold. “The July 2019 Ridgecrest, California, Earthquake Sequence: Kinematics of Slip and Stressing in Cross-Fault Ruptures.” *Geophysical Research Letters* 46, no. 21 (November 16, 2019): 11859–67. https://doi.org/10.1029 /2019GL084741.

Bartley, John, Allen Glazner, Drew Coleman, Andrew Kylander-Clark, Russell Mapes, and Anke Friedrich. “Large Laramide Dextral Offset across Owens Valley, California, and Its Possible Relation to Tectonic Unroofing of the Southern Sierra Nevada.” *Special Paper of the Geological Society of America* 434 (January 2007): 129. https://doi.org/10.1130/2007.2434(07).

Beanland, Sarah, and Malcolm M. Clark. “The Owens Valley Fault Zone, Eastern California, and Surface Faulting Associated with the 1872 Earthquake.” Report. Bulletin, 1994. USGS Publications Warehouse. https://doi.org/10.3133/b1982.

Bennett, R., Brian Wernicke, Nathan Niemi, Anke Friedrich, and James Davis. “Contemporary Strain Rates in the Northern Basin and Range Province from GPS Data.” *Tectonics* 22 (April 1, 2003): 1008. https://doi.org/10.1029/2001TC001355.

Burbank, Douglas W., and David P. Whistler. “Temporally Constrained Tectonic Rotations Derived from Magnetostratigiraphic Data: Implications for the Initiation of the Garlock Fault, California.” *Geology* 15, no. 12 (December 1, 1987): 1172–75. https://doi.org/10.1130 /0091-7613(1987)15<1172:TCTRDF>2.0.CO;2.

Butler, Paul Ray, Bennie W. Troxel, And Kenneth L. Verosub. “Late Cenozoic History and Styles of Deformation along the Southern Death Valley Fault Zone, California.” *GSA Bulletin* 100, no. 3 (March 1, 1988): 402–10. https://doi.org/10.1130 /0016-7606(1988)100<0402:LCHASO>2.3.CO;2.

Carter, Bruce, SF McGill, and TM Ross. “Neogene Offsets and Displacement Rates, Central Garlock Fault, California.” *Geological Investigations of an Active Margin*, 1994, 348–56.

Chuang, Ray Y., and Kaj M. Johnson. “Reconciling Geologic and Geodetic Model Fault Slip-Rate Discrepancies in Southern California: Consideration of Nonsteady Mantle Flow and Lower Crustal Fault Creep.” *Geology* 39, no. 7 (July 1, 2011): 627–30. https://doi.org/10.1130/G32120.1.

Davis, Gregory A., And B. C. Burchfiel. “Garlock Fault: An Intracontinental Transform Structure, Southern California.” *GSA Bulletin* 84, no. 4 (April 1, 1973): 1407–22. https://doi.org /10.1130/0016-7606(1973)84<1407:GFAITS>2.0.CO;2.

Dokka, Roy K., Michael J. Mahaffie, and Arthur W. Snoke. “Thermochronologic Evidence of Major Tectonic Denudation Associated with Detachment Faulting, Northern Ruby Mountains - East Humboldt Range, Nevada.” *Tectonics* 5, no. 7 (December 1, 1986): 995–1006. https://doi.org /10.1029/TC005i007p00995.

Dolan, James F., Lee J. McAuliffe, Edward J. Rhodes, Sally F. McGill, and Robert Zinke. “Extreme Multi-Millennial Slip Rate Variations on the Garlock Fault, California: Strain Super-Cycles, Potentially Time-Variable Fault Strength, and Implications for System-Level Earthquake Occurrence.” *Earth and Planetary Science Letters* 446 (2016): 123–36. https://doi.org/10.1016 /j.epsl.2016.04.011.

EarthScope Southern & Eastern California LiDAR Project. Distributed by OpenTopography. https://doi.org/10.5069/G9G44N6Q . Accessed: 2023-03-20 (SECLP, 2007).

Frankel, Kurt L., and James F. Dolan. “Characterizing Arid Region Alluvial Fan Surface Roughness with Airborne Laser Swath Mapping Digital Topographic Data.” *Journal of Geophysical Research: Earth Surface* 112, no. F2 (June 1, 2007). https://doi.org/10.1029/2006JF000644.

Frankel, Kurt L., Allen F. Glazner, Eric Kirby, Francis C. Monastero, Michael D. Strane, Michael E. Oskin, Jeffrey R. Unruh, et al. “Active Tectonics of the Eastern California Shear Zone.” In *Field Guide to Plutons, Volcanoes, Faults, Reefs, Dinosaurs, and Possible Glaciation in Selected Areas of Arizona, California, and Nevada*, edited by Ernest M. Duebendorfer and Eugene I. Smith, 0.Geological Society of America, 2008. https://doi.org/10.1130/2008.fld011(03).

Frankel, Kurt L., Lewis A. Owen, James F. Dolan, Jeffrey R. Knott, Zachery M. Lifton, Robert C. Finkel, and Thad Wasklewicz. “Timing and Rates of Holocene Normal Faulting along the Black Mountains Fault Zone, Death Valley, USA.” *Lithosphere* 8, no. 1 (February 1, 2016): 3–22. https://doi.org/10.1130/L464.1.

Ganev, Plamen, James Dolan, Kimberly Blisniuk, Mike Oskin, and Lewis Owen. “Paleoseismologic Evidence for Multiple Holocene Earthquakes on the Calico Fault: Implications for Earthquake Clustering in the Eastern California Shear Zone.” *Lithosphere* 2 (July 20, 2010): 287–98. https://doi.org/10.1130/L82.1.

Ganev, Plamen N., James F. Dolan, Sally F. McGill, and Kurt L. Frankel. “Constancy of Geologic Slip Rate along the Central Garlock Fault: Implications for Strain Accumulation and Release in Southern California.” *Geophysical Journal International* 190, no. 2 (August 1, 2012): 745–60. https://doi.org/10.1111/j.1365-246X.2012.05494.x.

Geyh, Mebus, and Helmut Schleicher. *Absolute Age Determination: Physical and Chemical Dating Methods and Their Application*. 1st ed. Springer Berlin, Heidelberg, 1990.

Glazner, Allen F., J. Douglas Walker, John M. Bartley, and John M. Fletcher. “Cenozoic Evolution of the Mojave Block of Southern California.” In *Geologic Evolution of the Mojave Desert and Southwestern Basin and Range*, edited by Allen F. Glazner, J. Douglas Walker, and John M.

Bartley, 195:0. Geological Society of America, 2002. https://doi.org/10.1130/0-8137-1195-9.19.

Guns, Katherine A., Richard A. Bennett, Joshua C. Spinler, and Sally F. McGill. “New Geodetic Constraints on Southern San Andreas Fault-Slip Rates, San Gorgonio Pass, California.” *Geosphere* 17, no. 1 (December 10, 2020): 39–68. https://doi.org/10.1130/GES02239.1.

Hanks, Thomas C. “The Age of Scarplike Landforms From Diffusion-Equation Analysis.” In *Quaternary Geochronology*, 313–38. AGU Reference Shelf, 2000. https://doi.org/10.1029/RF004p0313.

Hanks, Thomas C., Robert C. Bucknam, Kenneth R. Lajoie, and Robert E. Wallace. “Modification of Wave-Cut and Faulting-Controlled Landforms.” *Journal of Geophysical Research: Solid Earth* 89, no. B7 (July 10, 1984): 5771–90. https://doi.org/10.1029/JB089iB07p05771.

Hileman, J.A., C.R. Allen, and J.M. Nordquist. *Seismicity of the Southern California Region: 1 Jan. 1932 to 31 Dec. 1972*. Contribution - California Institute of Technology, Pasadena. Division of Geological and Planetary Sciences. Seismological Laboratory, California Institute of Technology, with assistance from the Earthquake Research Affiliates, 1973. https://books.google.com /books?id=NNcSAQAAIAAJ.

Hill, Mason L, And T. W Dibblee Jr. “San Andreas, Garlock, And Big Pine Faults, California: A Study Of The Character, History, And Tectonic Significance Of Their Displacements.” *GSA Bulletin* 64, no. 4 (April 1, 1953): 443–58. https://doi.org/10.1130/0016-7606(1953)64[443:SAGABP]2.0.CO;2.

Hoffman, William. “Late Pleistocene Slip Rates Along The Panamint Valley Fault Zone, Eastern California,” 2009.

Keenan, Deborah L. *The Geology and Geochemistry of Volcanic Rocks in the Lava Mountains, California: Implications for Miocene Development of the Garlock Fault*. University of Nevada, Las Vegas, 2000.

Kirby, Eric, Sridhar Anandakrishnan, Fred Phillips, and Shasta Marrero. “Late Pleistocene Slip Rate along the Owens Valley Fault, Eastern California.” *Geophysical Research Letters* 35, no. 1 (January 1, 2008). https://doi.org/10.1029/2007GL031970.

Kylander-Clark, Andrew, Drew Coleman, Allen Glazner, and John Bartley. “Evidence for 65 Km of Dextral Slip across Owens Valley, California, since 83 Ma.” *Geological Society of America Bulletin - GEOL SOC AMER BULL* 117 (July 1, 2005). https://doi.org/10.1130/B25624.1.

LaViolette, J.W., G.E. Christenson, and J.C. Stepp. “Quaternary Displacement on the Western Gatlock Fault, Southern California.” *Geology and Mineral Wealth of the California Desert*, 1980, 449–56.

Lee, Jeffrey, Joel Spencer, and Lewis Owen. “Holocene Slip Rates along the Owens Valley Fault, California: Implications for the Recent Evolution of the Eastern California Shear Zone.” *Geology* 29 (September 2001): 819–22. https://doi.org/10.1130 /0091-7613(2001)029<0819:HSRATO>2.0.CO;2.

Loomis, Dana P., And Douglas W. Burbank. “The Stratigraphic Evolution of the El Paso Basin, Southern California: Implications for the Miocene Development of the Garlock Fault and Uplift of the Sierra Nevada.” *GSA Bulletin* 100, no. 1 (January 1, 1988): 12–28. https://doi.org /10.1130/0016-7606(1988)100<0012:TSEOTE>2.3.CO;2.

Lubetkin, Lester K.C., And Malcolm M. Clark. “Late Quaternary Activity along the Lone Pine Fault, Eastern California.” *GSA Bulletin* 100, no. 5 (May 1, 1988): 755–66. https://doi.org /10.1130/0016-7606(1988)100<0755:LQAATL>2.3.CO;2.

McAuliffe, Lee J., James F. Dolan, Eric Kirby, Chris Rollins, Ben Haravitch, Steve Alm, and Tammy M. Rittenour. “Paleoseismology of the Southern Panamint Valley Fault: Implications for Regional Earthquake Occurrence and Seismic Hazard in Southern California.” *Journal of Geophysical Research: Solid Earth* 118, no. 9 (2013): 5126–46. https://doi.org/10.1002/jgrb.50359.

McGill, S F. “Late Quaternary Slip Rate of the Owl Lake Fault and Maximum Age of the Latest Event on the Easternmost Garlock Fault, S. California.” In *Geological Society of America, Abstracts with Programs; (United States)*, Vol. 25:5. United States, 1993. https://www.osti.gov/biblio/5099834.

McGill, Sally F., Joshua C. Spinler, John D. McGill, Richard A. Bennett, Michael A. Floyd, Joan E. Fryxell, and Gareth J. Funning. “Kinematic Modeling of Fault Slip Rates Using New Geodetic Velocities from a Transect across the Pacific-North America Plate Boundary through the San Bernardino Mountains, California.” *Journal of Geophysical Research: Solid Earth* 120, no. 4 (April 1, 2015): 2772–93. https://doi.org/10.1002/2014JB011459.

McGill, Sally F., Stephen G. Wells, Sarah K. Fortner, Heidi Anderson Kuzma, and John D. McGill. “Slip Rate of the Western Garlock Fault, at Clark Wash, near Lone Tree Canyon, Mojave Desert, California.” *GSA Bulletin* 121, no. 3–4 (March 1, 2009): 536–54. https://doi.org/10.1130/B26123.1.

McGill, Sally, and Kerry Sieh. “Holocene Slip Rate of the Central Garlock Fault in Southeastern Searles Valley, California.” *Journal of Geophysical Research: Solid Earth* 98, no. B8 (August 10, 1993): 14217–31. https://doi.org/10.1029/93JB00442.

Meade, Brendan J., and Bradford H. Hager. "Block Models of Crustal Motion in Southern California Constrained by GPS Measurements." *Journal of Geophysical Research: Solid Earth* 110, no. B3 (March 1, 2005). https://doi.org/10.1029/2004JB003209.

Miller, M. Meghan, Daniel J. Johnson, Timothy H. Dixon, and Roy K. Dokka. "Refined Kinematics of the Eastern California Shear Zone from GPS Observations, 1993-1998." *Journal of Geophysical Research* 109, no. B2 (February 10, 2001): 2245–63.

Monastero, F. C., A. E. Sabin, and J. D. Walker. "Evidence for Post-Early Miocene Initiation of Movement on the Garlock Fault from Offset of the Cudahy Camp Formation, East-Central California." *Geology* 25, no. 3 (March 1, 1997): 247–50. https://doi.org/10.1130 /0091-7613(1997)025<0247:EFPEMI>2.3.CO;2.

National Park Service, U.S. Department of the Interior. "Death Valley Weather," 2023.https://www.nps.gov/deva/planyourvisit/weather.htm.

Regmi, Netra R., Eric V. McDonald, and Steven N. Bacon. "Mapping Quaternary Alluvial Fans in the Southwestern United States Based on Multiparameter Surface Roughness of Lidar Topographic Data." *Journal of Geophysical Research: Earth Surface* 119, no. 1 (2014): 12–27. https://doi.org /10.1002/2012JF002711.

Renik, Byrdie, and Nicholas Christie-Blick. "A New Hypothesis for the Amount and Distribution of Dextral Displacement along the Fish Lake Valley–Northern Death Valley–Furnace Creek Fault Zone, California-Nevada." *Tectonics* 32, no. 2 (March 1, 2013): 123–45. https://doi.org/10.1029 /2012TC003170.

Rittase, William M., Eric Kirby, Eric McDonald, J. Douglas Walker, John Gosse, Joel Q.G. Spencer, and A.J. Herrs. "Temporal Variations in Holocene Slip Rate along the Central Garlock Fault, Pilot Knob Valley, California." *Lithosphere* 6, no. 1 (February 1, 2014): 48–58. https://doi.org/10.1130/L286.1.

Rockwell, Thomas, Timothy Dawson, Jeri Ben-Horin, and Gordon Seitz. "A 21-Event, 4,000-Year History of Surface Ruptures in the Anza Seismic Gap, San Jacinto Fault, and Implications for Long-Term Earthquake Production on a Major Plate Boundary Fault." *Pure and Applied Geophysics* 172 (May 1, 2015). https://doi.org/10.1007/s00024-014-0955-z.

Schermer, Elizabeth R., B. P. Luyendyk, and Stanley M. Cisowski. "Late Cenozoic Structure and Tectonics of the Northern Mojave Desert." *Tectonics* 15 (1996): 905–32.

Smith, Roger S.U. “Holocene Offset and Seismicity along the Panamint Valley Fault Zone, Western Basin-and-Range Province, California.” *Recent Crustal Movements* 52, no. 1 (February 10, 1979): 411–15. https://doi.org/10.1016/0040-1951(79)90256-7.

Snow, J. Kent, and Brian Wernicke. “Uniqueness of Geological Correlations: An Example from the Death Valley Extended Terrain.” *GSA Bulletin* 101, no. 11 (November 1, 1989): 1351–62. https://doi.org/10.1130/0016-7606(1989)101<1351:UOGCAE>2.3.CO;2.

Su, Qiang, Junjie Ren, Xianyan Wang, and Oubo Liang. “A Power-Law Relation of Surface Roughness and Ages of Alluvial Fans in a Hyperarid Environment: A Case Study in the Dead Sea Area.” *Progress in Physical Geography: Earth and Environment* 0, no. 0 (n.d.): 03091333221118641.https://doi.org/10.1177/03091333221118641.

Walker, J. Douglas, Adrian K. Berry, Patrick J. Davis, Joseph E. Andrew, and John M. Mitsdarfer. “Geologic Map of Northern Mojave Desert and Southwestern Basin and Range, California: Compilation Method and References.” In *Geologic Evolution of the Mojave Desert and Southwestern Basin and Range*, edited by Allen F. Glazner, J. Douglas Walker, and John M.Bartley, 195:0. Geological Society of America, 2002. https://doi.org/10.1130/0-8137-1195-9.295.

Zhang, Peizhen, Michael Ellis, D. B. Slemmons, and Fengying Mao. “Right-Lateral Displacements and the Holocene Slip Rate Associated with Prehistoric Earthquakes along the Southern Panamint Valley Fault Zone: Implications for Southern Basin and Range Tectonics and Coastal California Deformation.” *Journal of Geophysical Research: Solid Earth* 95, no. B4 (1990): 4857–72. https://doi.org/10.1029/JB095iB04p04857.